Microstructure and very high cycle fatigue characteristics of powder bed fused – laser beam (PBF-LB) scandium-free Al-Mg-Zr alloy

Original
Microstructure and very high cycle fatigue characteristics of powder bed fused – laser beam (PBF-LB) scandium-free Al-Mg-Zr alloy / Shakil, S.I., Bednarczyk, W., Gajewska, M., Mahbooba, Z., Saharan, A., Tridello, A., Paolino, D.S., Haghshenas, M.. - In: MATERIALS SCIENCE AND ENGINEERING A-STRUCTURAL MATERIALS PROPERTIES MICROSTRUCTURE AND PROCESSING. - ISSN 0921-5093. - 930:(2025). [10.1016/j.msea.2025.148177]

Publisher:
Elsevier

Published
DOI:10.1016/j.msea.2025.148177

Materials Science & Engineering A 930 (2025) 148177

Contents lists available at ScienceDirect

Materials Science & Engineering A

journal homepage: www.elsevier.com/locate/msea

Microstructure and very high cycle fatigue characteristics of powder bed fused – laser beam (PBF-LB) scandium-free Al-Mg-Zr alloy

Shawkat I. Shakil [a], Wiktor Bednarczyk [b], Marta Gajewska [c], Zaynab Mahbooba [d], Ankit Saharan [d], Andrea Tridello [e], Davide S. Paolino [e], Meysam Haghshenas [a,*]

[a] Fatigue, Fracture, and Failure Laboratory (F3L), University of Toledo, Toledo, OH, 43606, USA
[b] Faculty of Metals and Industrial Computer Science, AGH University of Krakow, al. A. Mickiewicza 30, 30-059, Krakow, Poland
[c] Academic Centre for Materials and Nanotechnology, AGH University of Krakow, al. A. Mickiewicza 30, 30-059, Krakow, Poland
[d] EOS North America Inc., Pflugerville, TX, USA
[e] Department of Mechanical and Aerospace Engineering, Politecnico di Torino, Turin, Italy

ARTICLE INFO

Keywords:
VHCF
Ultrasonic fatigue
Additive manufacturing
PBF-LB
Al-Mg-Zr
EOS 5X1

ABSTRACT

This study investigates the microstructure and very high cycle fatigue (VHCF) behavior of a powder bed fusion–laser beam (PBF-LB) processed scandium-free Al-Mg-Zr alloy (commercially known as EOS Al5X1) through advanced microstructural characterization, defect analysis, ultrasonic fatigue testing, and detailed fractographic examination. The analysis focuses on defect-driven crack initiation, particularly process-induced volumetric defects such as pores, lack of fusion, and non-metallic (oxide) inclusions. Scanning electron microscopy-based fractography reveals that in the VHCF regime, where the number of cycles to failure (N_f) > 10^7 cycles, fatigue crack initiation predominantly shifts toward the subsurface or interior of the specimen. In multiple cases, process-induced volumetric defects facilitated crack initiation, resulting in characteristic 'fisheye' fracture morphologies. The chemical composition of these critical defects was also analyzed in detail. The study highlights the significant impact of process-induced volumetric defects on fracture morphology and examines the influence of defect size and location on VHCF performance. These findings provide deeper insight into the interplay between processing defects and crack nucleation, underscoring the necessity of advanced defect characterization to better understand VHCF life variability.

1. Introduction

Very high cycle fatigue (VHCF) is a critical consideration in evaluating the durability and performance of alloys, especially in demanding applications such as aerospace and high-speed trains, where components frequently experience cyclic loading beyond 10 million cycles, surpassing the traditional fatigue limit. Notably, the updated United States Air Force Engine Structural Integrity Program (ENSIP) mandates that all jet engine components must demonstrate a minimum fatigue life of 10^9 cycles, underscoring the necessity for advanced materials and precise fatigue characterization to meet stringent durability requirements [1–3]. There is no infinite fatigue life in metallic materials [4] and under these cyclically demanding conditions, the sustained mechanical integrity and reliability of materials become particularly critical when exposed to a very high number of low-stress amplitude cyclic loadings. For aluminum alloys, especially those produced via additive manufacturing (AM) processes, understanding VHCF behavior is essential due to aluminum's widespread use in lightweight, high-strength, and fatigue-critical applications [5–7]. These alloys must exhibit not only desirable mechanical properties but also exceptional fatigue resistance to ensure longevity and safety in service. Investigating the VHCF behavior of AM aluminum alloys is thus vital to optimize their performance and validate their suitability for safety-critical applications.

However, the utilization of traditional high-strength aluminum alloys, such as the 2xxx and 7xxx series, is often limited by their non-fusion weldable nature and the challenges posed by hot cracking during solidification [8–11]. While Al-Mg 5xxx alloys offer improved weldability, they fall short of achieving significant strength enhancements through heat treatment [12,13]. A significant advancement in this field is the development of Scalmalloy, an Al-Mg alloy strengthened with scandium (Sc) and zirconium (Zr), which possesses age-hardening

---

* Corresponding author.
E-mail address: meysam.haghshenas@utoledo.edu (M. Haghshenas).

https://doi.org/10.1016/j.msea.2025.148177
Received 15 December 2024; Received in revised form 15 February 2025; Accepted 5 March 2025

properties ideal for fusion-based additive manufacturing processes [12,13]. Nevertheless, the high cost of scandium restricts its broader adoption, driving interest toward alternative Sc-free Al-Mg-Zr alloy systems that maintain desirable mechanical properties without the high cost [14–16].

Recent studies [17–19] indicate that Sc-free Al-Mg-Zr alloys are promising candidates for AM due to their favorable mechanical properties and processing characteristics. These alloys are characterized by a bimodal grain structure comprised of a fine grain zone (FGZ) and a coarse grain zone (CGZ), which contribute to their overall strength and ductility [17,20]. The FGZ typically consists of submicron grains with little to no texture, while the CGZ exhibits a weak {001} <100> fiber texture, influenced by the presence of primary Al_3Zr nano-precipitates [17,20]. Thermal treatments can further enhance these properties by promoting the formation of secondary $L1_2$-Al_3Zr precipitates, which significantly contribute to precipitation hardening [17,19,20]. Reports indicate that Sc-free Al-Mg-Zr alloys can achieve ultimate tensile strengths of approximately 450 MPa, with elongation values reaching up to 24 % [17]. The combination of cost-effectiveness and robust mechanical properties makes these alloys particularly attractive for industries requiring high performance and safety.

Despite these promising attributes, powder-based AM processes like powder bed fusion–laser beam (PBF-LB) can introduce defects such as lack of fusion (LoFs) and residual stresses, which critically impact the structural integrity of components under dynamic loading [21–24]. These defects often act as initiation sites for fatigue damage, leading to sudden and unpredictable failures, especially in the aerospace and automotive sectors [25,26]. Understanding the VHCF behavior of PBF-LB Al-Mg-Zr alloys is therefore essential for ensuring the reliability and safety of these materials in applications where long fatigue life is paramount. Exploring the relationship between microstructure, defects, and fatigue performance will provide key insights into the material's behavior under cyclic loading, ultimately aiding the design of components that meet stringent performance standards.

Recent studies have investigated the fatigue performance of PBF-LB Al-Mg-Zr alloys, providing insights into their high-cycle fatigue (HCF) behavior. In a previous work by the authors [27], the HCF performance of a PBF-LB Al-Mg-Zr-Mn alloy was evaluated, demonstrating a fatigue strength of approximately 140 MPa at 5 million cycles. The study highlighted the influence of defects and microstructure on fatigue behavior, emphasizing the role of the size and location of defects affecting fatigue resistance. Nezhadfar et al. [28] examined the fatigue behavior of PBF-LB aluminum alloys, including an AD1 alloy (Al-Mg-Zr, equivalent to EOS Al5X1), and reported that refined microstructures significantly improved fatigue resistance in HCF regimes. Their findings suggest that process-induced defects remain a primary limitation in extending fatigue life. Beyond PBF-LB-processed Al-Mg-Zr alloys, there have been additional studies on the fatigue performance of Sc- and Zr-modified Al-Mg alloys, including some studies conducted in hot isostatic pressing (HIP) condition. Hua et al. [29] examined the HCF properties of a PBF-LB Al-Mg-Sc-Zr alloy, revealing that fatigue failure was predominantly influenced by the distribution of defects such as lack of fusion and gas porosity. Similarly, He et al. [30] studied an Al-5024 alloy containing Sc and Zr, demonstrating that fatigue strength and yield strength were closely correlated, with a maximum fatigue strength of 105 MPa at 10^7 cycles following the strength increment and defect minimization through HIP treatment. Further work by Qin et al. [31,32] reinforced these findings, showing that defect morphology and size distribution play a crucial role in fatigue initiation. These studies collectively underscore the importance of minimizing defects during processing and post-processing to enhance the fatigue performance of PBF-LB Al-Mg alloys modified by Zr and/or Sc. While these works provide valuable insights into the fatigue behavior of Zr- and Sc-modified aluminum alloys, the VHCF response (where the number of cyclic loadings, N_f, is beyond 10^7 cycles) of PBF-LB Sc-free Al-Mg-Zr alloys (or PBF-LB Al-Mg alloys in general) remains largely unexplored, necessitating further investigation.

As the demand for lightweight and durable materials continues to grow, particularly in safety- and fatigue-critical applications such as aerospace, automotive, and structural engineering, understanding the fatigue behavior of PBF-LB Sc-free Al-Mg-Zr alloys, especially within the VHCF regime, becomes increasingly important. These applications require materials that can withstand prolonged cyclic loading without compromising structural integrity. By studying how these alloys respond to cyclic stress over extended periods, one can develop design guidelines that enhance the performance/reliability of demanding environments. Additionally, these insights will aid in optimizing AM processing parameters to consistently achieve the desired mechanical properties, such as strength and ductility, while minimizing the risk of fatigue-related failures.

Though the mentioned studies have quantified the conventional fatigue of PBF-LB Al-Mg-Zr alloys up to 5×10^6 or 10^7 cycles using servo-hydraulic fatigue testers, the ultra-long-life fatigue (i.e., VHCF regime where $N_f > 10^7$ cycles) of PBF-LB scandium-free Al-Mg-Zr alloys, assessed using ultrasonic fatigue testing approach, remains an under-explored area. This study will focus on key aspects of extended fatigue performance in the VHCF regime, beginning advanced microstructural characterization and process-caused defect analysis to quantify unique microstructural features of PBF-LB Al-Mg-Zr alloys, such as grain structure (size, distribution, and morphology) and the presence of PBF-LB-induced volumetric defects (e.g., lack of fusion). These factors significantly influence VHCF performance, particularly the mechanisms governing crack initiation, which are critical for predicting the material's long-term durability in practical applications. Additionally, this investigation will provide quantitative data on fatigue damage accumulation across varying stress levels and cycle counts, leading to the establishment of S-N data beyond the classic fatigue limit associated with 10^7 cycles. This foundational data will aid in evaluating the VHCF limit (strength) and overall performance of PBF-LB scandium-free Al-Mg-Zr alloys compared to traditional wrought Al-Mg alloys [33–35]. Finally, applying principles of fracture mechanics will enhance the understanding of VHCF crack behavior, allowing for a comprehensive assessment of these materials' reliability in real-world conditions.

2. Experimental procedure

2.1. Processing

In this study, the test specimens were fabricated using an Al-Mg-Zr alloy, commercially designated as EOS Al5X1 [36]. The alloy powder was produced via gas atomization, resulting in a particle size distribution characterized by $D_{10} = 31$ μm, $D_{50} = 45$ μm, and $D_{90} = 64$ μm. These parameters denote the particle diameters at which 10 %, 50 %, and 90 % of the cumulative particle volume is smaller, respectively. D_{10} represents the diameter below which 10 % of the cumulative particle volume lies, D_{50} (the median particle size) is the diameter below which 50 % of the cumulative volume lies, and D_{90} is the diameter below which 90 % of the cumulative particle volume lies. These values provide a concise summary of the range and variation of particle sizes in the sample.

The specimens were produced using an EOS M290 machine, operating with a laser power range of 350–400 W, a scan speed of 1000–1500 mm/s, a hatch distance of 0.10–0.12 mm, and a layer thickness of 40 μm. These parameters were presented as ranges to reflect the optimization process employed in this study. The ranges indicate the variability in the process conditions explored to achieve the best possible results for the alloy. For instance, the laser power and scan speed were adjusted to minimize magnesium (Mg) evaporation, considering Mg's low boiling point. By reporting ranges, this study provides a comprehensive understanding of the experimental conditions and highlights the flexibility required to fine-tune the process for optimal alloy performance. This approach ensures the findings apply to a broader set of conditions and can be replicated in different settings.

Based on the specified ranges of processing parameters, the volumetric energy density (VED) ranged from 48.6 J/mm^3 to 83.3 J/mm^3, depending on the specific parameter combinations used during optimization. The process achieved a build rate of 4.8 mm^3/s, with argon gas employed as a shielding medium to maintain an inert atmosphere and prevent oxidation. After printing, an aging heat treatment was performed by heating the specimens to 400 °C for 6 h, followed by gas quenching.

The chemical composition of both the alloy powder and the PBF-LB-processed specimens was determined using a combination of inductively coupled plasma (ICP) analysis for metallic elements and gas fusion analysis for non-metallic elements such as hydrogen, oxygen, and nitrogen. These analyses were conducted following recognized industry standards: ASTM E1479/E2371/E2823 for ICP and ASTM E1019/E1409/E2792 for gas fusion. The powder's chemical composition (in wt. %) included 2.5–4.2 % magnesium (Mg), 0.6–1.8 % zirconium (Zr), and 0.1–1.0 % manganese (Mn), along with minor impurities (<0.1 %) of iron (Fe), silicon (Si), and titanium (Ti) in an aluminum matrix. The specific chemical composition of the alloying elements, along with the impurity levels, measured from the PBF-LB-processed specimens using ICP and gas fusion analysis, are summarized in Table 1.

2.2. Microstructural assessment

After printing and post-heat treatment, small samples were prepared for microstructural analysis using standard metallographic techniques. The samples were mechanically ground and polished to ensure surface quality suitable for scanning electron microscopy (SEM) and electron backscatter diffraction (EBSD). Final polishing was completed electrolytically with a solution of 30 % HNO_3 in methanol at −30 °C under 20 V. Thin foils for transmission electron microscopy (TEM) were ground to ~100 μm, then electropolished using a Struers TenuPol twin-jet system under similar conditions.

SEM observations were performed on two orthogonal planes relative to the build direction, using a Hitachi SU-70 field emission SEM with a Bruker Quantax eFlashHD EBSD detector. Backscattered electron (BSE) imaging was conducted at 10 kV, and EBSD data were collected with both large (320×240 μm, 250 nm step size) and small (50 × 38 μm, 100 nm step size) maps to capture overall and detailed microstructural features. The analysis was based on the Hough transform method and focused on the Al (Fm-3m) phase, as second-phase precipitates were too small for effective EBSD resolution.

TEM analysis was carried out with an FEI Tecnai TF20 X-TWIN field emission gun microscope, operating at 200 kV. Imaging modes included high-resolution TEM (HRTEM), dark field (DF), bright-field (BF), and high-angle annular dark field (HAADF), with energy-dispersive spectroscopy (EDS) used for elemental analysis. The microscope employed a low-background double tilt holder to ensure accurate sample positioning and average background subtraction filtering (ABSF) was applied to enhance HRTEM image quality.

Advanced X-ray computed micro-tomography (XCT) scans were performed on aged PBF-LB Al-Mg-Zr specimens using a specialized system located in the J-Tech@PoliTO laboratories. This system was equipped with a 300 kV X-ray source that achieved a minimum focal spot size of 5 μm, paired with a 2048×2048-pixel flat panel detector to ensure high-resolution imaging. The primary goal of these scans was to identify and quantify volumetric defects within the gauge sections of fatigue test coupons. To optimize image resolution, the distance between the X-ray source and the detector was carefully adjusted. After scanning, the specimens were reconstructed into three-dimensional models using VG MAX 3.5 software from Volume Graphics GmbH in Heidelberg, Germany. Subsequently, a dedicated software module was utilized for defect detection and analysis, allowing for precise measurement and evaluation of internal imperfections within the specimens.

Table 1
Chemical composition of the studied PBF-LB Al5X1 specimens.

Element	Weight Percent (wt.%)	Classification
Mg	3.50	Alloying element
Zr	1.38	Alloying element
Mn	0.40	Alloying element
Si	0.12	Impurity
Fe	0.08	Impurity
Ti, Cu, Ni, Zn	<0.01	Impurity
H, N	<0.01	Impurity
O	0.03	Impurity
Al	Balance	Matrix

2.3. Quasistatic uniaxial tensile testing

Quasistatic uniaxial tensile tests were conducted, following the ASTM E8 standard, on the studied material (i.e., aged PBF-LB Al-Mg-Zr alloy) in the machined condition. A servo-hydraulic MTS system with a load capacity of 100 kN was used to carry out all the tests. The tensile load was applied vertically, parallel to the build direction, at a uniform strain rate of 10^{-3} s^{-1}. The tensile test results (e.g., 0.2 % offset stress) were taken as a baseline to design the fatigue stress levels at various percentages of yield strength.

2.4. Ultrasonic fatigue (USF) testing

The fully reversed ($R = -1$) VHCF performance of the material was evaluated using ultrasonic fatigue (USF) testing. This testing methodology facilitates the investigation of material behavior under cyclic loading conditions reaching up to 10^9 cycles, which is particularly relevant for applications requiring long-term durability. The USF testing employs a piezoelectric converter that converts electrical energy into mechanical vibrations, producing cyclic stresses at a high frequency of 20 kHz. An eddy current sensor is integrated into the setup to measure the displacement of the vibrating specimen, achieved by detecting changes in the surrounding magnetic field. This displacement is directly related to the applied mechanical load, enabling the accurate calculation of stress amplitudes throughout the testing process.

For this study, all tests were conducted on the aged specimens using a USF-2000A (Shimadzu) testing machine, a high-precision device tailored for VHCF research. Both the calibration rod and the test specimens were meticulously machined to resonate at the specified frequency of 20 kHz, ensuring the reliability and reproducibility of the experimental conditions. The resonant frequency of the specimens was calculated based on the material's intrinsic properties, including the measured Young's modulus and density, which directly influence their vibrational behavior. The precise dimensions of the calibration rod and test specimens were critical in achieving the desired resonance and ensuring optimal performance during the USF tests.

The specimen geometry, with all dimensions after machining, is shown in Fig. 1. All specimens, fabricated in the vertical build orientation, underwent sequential mechanical polishing using sandpapers ranging from 3000 grit to 7000 grit, ensuring a mirror-like surface finish. The polishing steps primarily removed micro-scratches and minimized surface imperfections that could otherwise influence fatigue performance.

Throughout the testing process, the temperature of the specimens was carefully monitored using a laser thermometer (Infrared Thermometer, ETEKCITY Lasergrip 1022D), with a maximum allowable temperature increase of 40 °C to prevent thermal effects from influencing the fatigue data. To minimize self-heating, compressed air was directed at the gauge section of the specimens, and testing was conducted using intermittent driving (i.e., pulse and pause sequences with a pulse duration of 300 ms followed by a pause of 200 ms). The compressed air cooling along with intermittent driving was consistently effective, for all specimens tested at all stress levels, in the elimination of self-heating concerns.

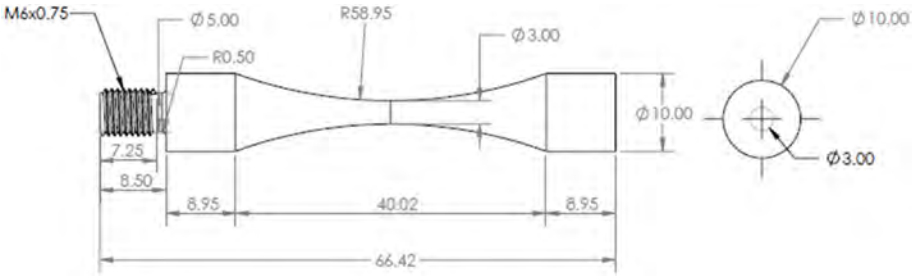

Fig. 1. Dimensions of the USF hourglass test specimen (after machining).

Stress amplitude levels for fatigue testing were selected based on tensile and conventional fatigue tests. Tensile tests provided the alloy's 0.2 % offset stress (390 MPa), and conventional fatigue tests were conducted at various percentages of the tensile yield stress, covering fatigue lives up to 5×10^6 cycles [27]. From these results, stress levels for VHCF testing were chosen to extend fatigue lives to 10^9 cycles, ranging from 78 MPa to 156 MPa (20 %–40 % of the yield (0.2 % offset) stress). After the test, the fatigue fractured surfaces were thoroughly examined using fractographic techniques to identify the mode of fatigue crack initiation and propagation. This analysis employed a Keyence VHX-600 Digital Microscope and an FEI Quanta 3D FEG SEM. This comprehensive methodology enabled an in-depth assessment of fatigue behavior, examining all fatigue-fractured specimens to gain insights into the crack initiation sites and propagation mechanisms.

3. Results and discussion

3.1. Microstructural characterization

A detailed microstructural investigation of the PBF-LB Al-Mg-Zr alloy was conducted, examining the distribution of grains, local lattice misorientation, and crystallographic orientation/texture using SEM-based imaging and EBSD technique.

Fig. 2 illustrates a representative scanning electron micrograph of the XZ cross-section. The microstructure reveals two distinct grain morphologies: equiaxed and columnar grains. The equiaxed grains are predominantly located along the boundaries of the melt pool, where the cooling rates are likely higher, promoting finer and more uniform grain growth. The columnar grains are found within the central regions of the melt pool, between the melt pool boundaries, and exhibit an orientation nearly perpendicular to these boundaries. This alignment of columnar grains suggests directional solidification driven by the thermal gradient during the solidification process.

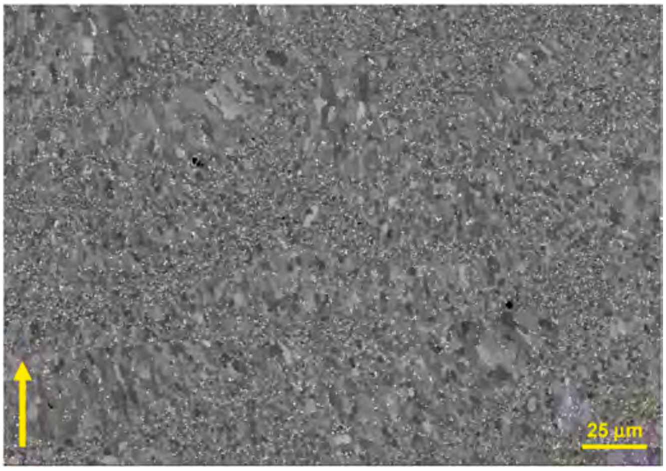

Fig. 2. SEM image of the starting microstructure showing grains in the melt pool and melt pool boundaries. The yellow arrow shows the build direction. (For interpretation of the references to color in this figure legend, the reader is referred to the Web version of this article.)

Fig. 3a presents the image quality (IQ) or band contrast (BC) map of the studied PBF-LB Al-Mg-Zr alloy (post-aged), which provides a detailed visualization of the grain structure by highlighting differences in the sharpness and clarity of Kikuchi diffraction patterns generated during EBSD scans. The bimodal grain structure is distinguishable, with fine equiaxed grains at the melt pool boundaries (fine grain zone, FGZ) and larger grains within the melt pool (coarse grain zone, CGZ). The grain size distribution in Fig. 3b quantitatively presents the bimodal patten using color-coded grains, with an average grain size of 2.62 ± 1.47 µm. The FGZ predominantly consists of grains under ~2 µm, while the CGZ contains grains averaging around 5 µm. The rapid cooling inherent in the PBF-LB process plays a crucial role in refining the grains of the Al-Mg-Zr alloy, with the formation of a bimodal grain structure strongly influenced by the distribution of primary Al_3Zr precipitates. Near the melt pool boundaries, the high concentration of Zr precipitates promotes fine equiaxed grains by acting as potent nucleation sites and by limiting grain growth through grain boundary pinning [17,19]. This pinning effect is effective because the precipitates inhibit the mobility of grain boundaries, preventing excessive growth. However, moving toward the core of the melt pool, the availability of Zr precipitates diminishes, leading to fewer nucleation sites and reduced grain boundary pinning. This reduction grants more freedom for grain growth, resulting in coarser grains within the melt pool interior. Such spatial variations in microstructure, characterized by fine grains in regions with higher Zr precipitate concentration and larger grains in areas with reduced precipitate density, are well-documented in Zr/Sc modified PBF-LB aluminum alloys [17,20,37,38]. The bimodal grain structure may contribute to mechanical anisotropy in the alloy [31,39,40] and influence the strength-ductility balance as the fine grains near the boundaries enhance strength, while larger grains in the core regions promote ductility [17,41,42]. Fig. 3c presents the Kernel average misorientation (KAM) map, illustrating local variations in lattice misorientation within the alloy. A distinct band of higher misorientation, shown in bright yellow, highlights regions with higher misorientations/elevated dislocation density. The high-misorientation areas can contribute to strain hardening, enhancing strength, but they can also act as stress concentration sites, which may impact fatigue resistance [43–45]. The map shows both high-angle grain boundaries (HAGBs) and low-angle grain boundaries (LAGBs). HAGBs contribute to strength by limiting grain boundary sliding, while LAGBs, within large grains, indicate areas of localized lattice strain. Overall, the KAM map does not display significant variations in strain distribution across the grain structure which can be attributed to the stress relieving during the post-aging treatment. In Fig. 3d, the inverse pole figure (IPF) map illustrates the crystallographic orientation of the grains along three basic crystallographic directions of the FCC material. The map indicates a nearly random orientation of the grains.

The pole figures presented in Fig. 4 depict the crystallographic texture of the studied alloy along the build direction. Given the low multiples of random distribution (MRD) value of approximately 1.77, it

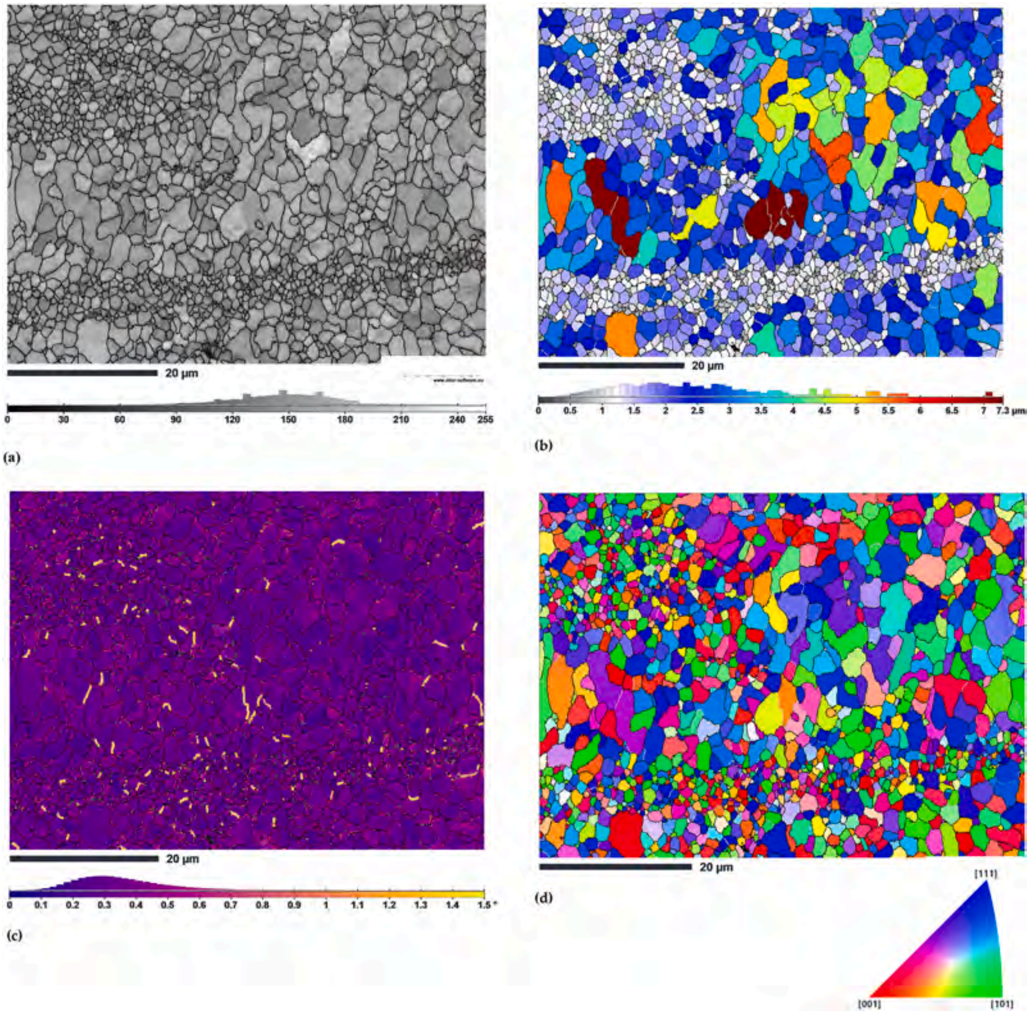

Fig. 3. (a) EBSD Image Quality (IQ) map of the PBF-LB Al-Mg-Zr alloy (post-aged); (b) Grain size distribution map showing variations in grain size across the microstructure; (c) Kernel Average Misorientation (KAM) map highlighting local misorientation variations associated with dislocation density; (d) Inverse Pole Figure (IPF) map representing the crystallographic orientation of grains.

is indeed indicative of a weak or nearly random texture in the studied alloy. The low MRD aligns with a minimally preferred crystallographic orientation, meaning the grains are distributed with a relatively random orientation. This weak texture is not uncommon in materials processed by PBF-LB, especially if the processing parameters (e.g., scan strategy, build temperature) were designed to minimize directional solidification effects, promoting more isotropic properties. Therefore, the structure is indeed weakly textured and can be reasonably classified as a texture-less structure. Fig. 5 further shows the texture of the PBF-LB Al-Mg-Zr alloy along the X, Y, and Z directions using IPF stereographic triangles. Each triangle displays the distribution of grain orientations relative to these axes. The color gradient, ranging from blue to red, represents the MRD values, with red areas indicating a higher density of grains oriented in specific crystallographic directions and blue areas showing more random orientations. In all three directions (X, Y, and Z), the MRD values remain close to 1.0, indicating a weak or nearly random texture across the alloy. The slight orientation preference seen near the (101) planes comes from the orientation preference of a few larger grains present in the CGZ. This weak texture implies that the material has nearly isotropic properties, making it suitable for applications requiring consistent mechanical behavior in multiple directions.

To investigate the distribution and composition of fine precipitates within the PBF-LB Al-Mg-Zr alloy, TEM imaging combined with EDS analysis was conducted, and the results are shown in Fig. 6. Fig. 6a and b shows BF and HAADF images of microstructure typical for the FGZ, where the distribution of nanoprecipitates is visible. Homogeneous distribution of precipitates can be observed with a large part of the particles located within grain boundaries (indicated by blue arrows). Such accumulation of precipitates along grain boundaries enhances mechanical properties by strengthening the grain boundaries and restricting slip [17,18,46]. Occasionally, larger precipitates can be seen within grain interiors, appearing brighter than the Al matrix in HAADF contrast, indicating Zr or Mn-rich phases. These precipitates enhance the alloy's mechanical properties by limiting grain boundary mobility and dislocation motion thus also improving its strength. Fig. 6c provides a BF TEM image of a single aluminum grain, where a dense dispersion of nanoscale Zr-rich precipitates (i.e., Al_3Zr) is evident. These precipitates are distributed throughout the grain and can also effectively hinder dislocation movement and contribute to hardening.

The blue box in Fig. 6c marks the area selected for EDS mapping to determine the elemental distribution in detail. The corresponding EDS maps are shown in Fig. 6d, displaying distributions for Al, Mg, Mn, Zr, and O. The Al (green) and Mg (orange) maps show a uniform distribution across the grain, indicating the formation of the primary matrix (i.e., Al-Mg solid solution). The large precipitate located at the center of the EDS map appears darker on both Al and Mg maps, indicating depletion. On the other hand, the increase in intensity visible on the Mn EDS map, as well as the O (red) map, confirms that the hexagonal particle is a discrete intragranular Mn-rich oxide. The apparent oxidation of manganese, which leads to the formation of stable oxide inclusions may

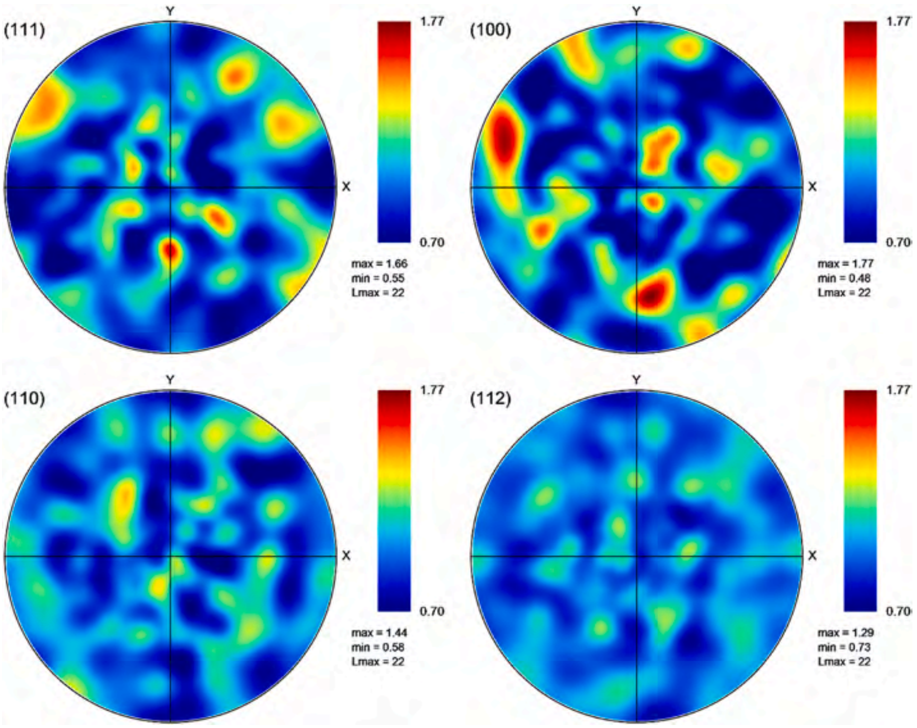

Fig. 4. EBSD pole figures illustrating the texture from different crystallographic planes of the PBF-LB Al-Mg-Zr alloy (post-aged), revealing insignificant texture, with the strongest texture observed on (100) pole figure, that signifies the preferred orientation of (100) planes of the coarse grains along {001} and {011} directions.

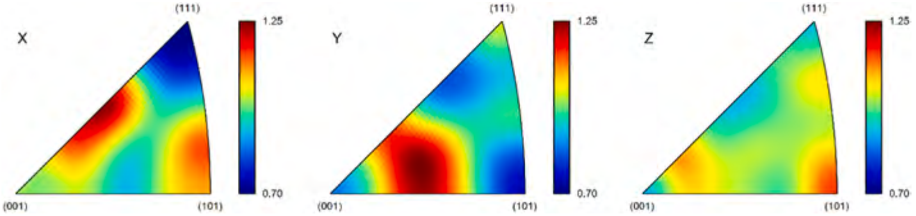

Fig. 5. Pole figure with stereographic triangles showing the weak crystallographic texture of the PBF-LB Al-Mg-Zr alloy (post-aged) along the X, Y, and Z directions.

also contribute to microstructural stability/strengthening of the alloy. These oxides also act as sites for dislocation pinning, though they may also act as potential sites for crack initiation under cyclic loading.

The Zr (purple) distribution map reveals a high density of nano-sized Zr-rich precipitates. HR imaging combined with FFT analyses allowed us to confirm that they are Al_3Zr particles with an ordered FCC ($L1_2$) structure, as shown in Fig. 6e. They were found to be coherent with the Al matrix, which is due to only a slight mismatch of their lattices, resulting in low interfacial energy and low strain. Such precipitates play a vital role in enhancing the alloy's strength and fatigue resistance by pinning grain boundaries and impeding dislocation motion [20,47]. The beneficial influence of the coexistence of coherent and incoherent precipitates manifests itself in more homogeneous deformation, thus preventing local strain concentration and early cleavage cracking.

3.2. Volumetric defect distribution

The XCT scan performed on the gauge section of the fatigue test specimen quantified a relative density of 99.91 %. As depicted in Fig. 7a, numerous defects were observed, with equivalent spherical diameters ranging from 13 μm to 83 μm. The close-up views in the additional images in Fig. 7b show the largest defect from XY, YZ, and XZ planes along with a magnified view of the defect distribution at the bottom right corner of Fig. 7b. Similarly, Fig. 7c shows a magnification of the inspected specimen close to the specimen center. The peak stress in hourglass specimens is reached at the specimen center, with the stress amplitude rapidly decreasing as the specimen ends approached. Therefore, the region at the minimum diameter is expected to be critical in the crack nucleation process. As seen in Fig. 7c, a significant number of defects are present in this cross-section, but they are not the largest found within the specimens. A bar chart in Fig. 7d illustrates the defect size distribution, showing that most defects are small (10–20 μm), while larger defects, though fewer, are generally expected to have a greater impact on fatigue behavior. However, the crack initiation process depends on the defect size and the applied stress and, when the stress amplitude varies rapidly along the specimen length, the largest defect may not be the most critical. This has been confirmed through the detailed analysis of the fracture surfaces described in the next sections.

The larger defects, highlighted in red, represent critical defects with sizes exceeding 60 μm, which are more likely to influence fatigue life. These defects, including a maximum defect size of 83 μm, are rare but crucial in determining crack initiation and propagation under cyclic loading. The defect size distribution presented in Fig. 7d shows that as the defect size increases, the density of these defects decreases significantly. This suggests that while the material has many small defects that may not be critical under VHCF conditions, the larger defects could still play a dominant role in fatigue failure, which could result in early crack initiation and reduce the material's overall fatigue life. This observation emphasizes the need to minimize such defects during the fabrication process to improve the fatigue performance of scandium-free PBF-LB Al-

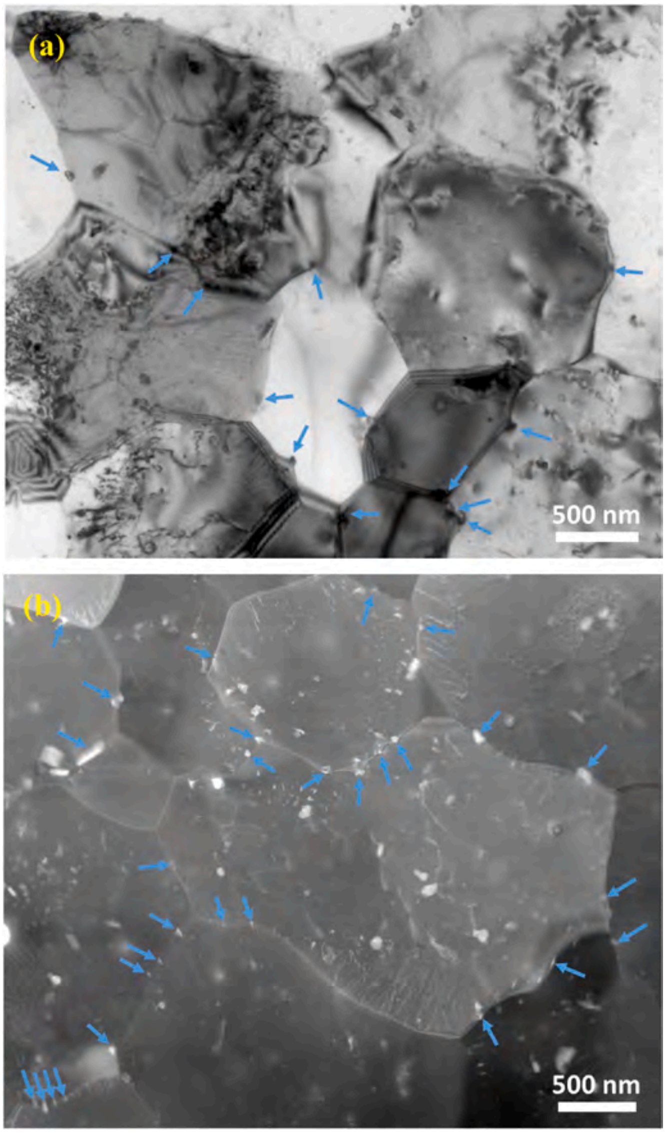

Fig. 6. (a) BF TEM and (b) HAADF images of the PBF-LB Al-Mg-Zr alloy (post-aged) showing the distribution of precipitates in the FGZ, blue arrows indicate precipitates located in grain boundaries, (c) BF TEM image of a single grain filled with nanoscale Zr-rich precipitates, with the yellow box marking the EDS scan location, (d) corresponding EDS maps for Al, Mg, Mn, Zr, and O, showing a high number density of Zr-rich precipitates within the grain and an isolated Mn-rich oxide particle and (e) HR image showing fine Al_3Zr precipitates inside Al grain along with color boxes marking areas of FFT analyses (insets) confirming their $L1_2$ structure and coherency with matrix. (For interpretation of the references to color in this figure legend, the reader is referred to the Web version of this article.)

Mg-Zr alloys for fatigue-critical applications.

Fig. 8 plots the sphericity concerning the equivalent diameter of the defects found in the specimen inspected with the XCT equipment. The sphericity index can be considered a reliable complexity factor associated with defects since it quantifies how closely the geometry of a defect approaches the geometry of a spherical defect (sphericity equal to 1). According to Fig. 8, the degree of complexity associated with the defect geometry tends to increase as the defect equivalent diameter increases. This trend is quite in agreement with the literature [48], confirming that larger defects are more likely to be characterized by more complex shapes and geometries.

It must be noted that the specimen inspected with the XCT equipment has not been tested. The XCT analysis provides reliable indications of the defect size range and spatial distribution, but it does not aim to correlate the defect size and the crack initiation process or the specimen failure. Indeed, with XCT inspections, the criticality associated with each defect can be hardly defined, since, according to Ref. [48], the largest defect may not be the most critical one (killer defect). On the other hand, the nature (e.g., composition) of “killer” defect(s) on the fracture surfaces has been thoroughly investigated in Section 3.5, to assess the correlation between the defectsg features (size, type, and location) and the VHCF response of the investigated material.

3.3. Mechanical properties

Quasistatic uniaxial tensile testing was conducted on the dog-bone tensile specimens (3 tests for the sake of reproducibility) of the studied aged PBF-LB Al-Mg-Zr-Mn alloy, and the average stress-strain (flow) curve is presented in Fig. 9. The PBF-LB Al-Mg-Zr-Mn alloy exhibits a 0.2 % offset (yield) stress of 390 ± 2 MPa, an ultimate tensile strength (UTS) of 428 ± 2 MPa, and an elongation to failure of 14.26 ± 0.94 %.

As seen, the tensile flow curve is characterized by a yield point elongation plateau up to approximately 3 % strain without a proportional stress increase [49]. This behavior is attributed to a limited

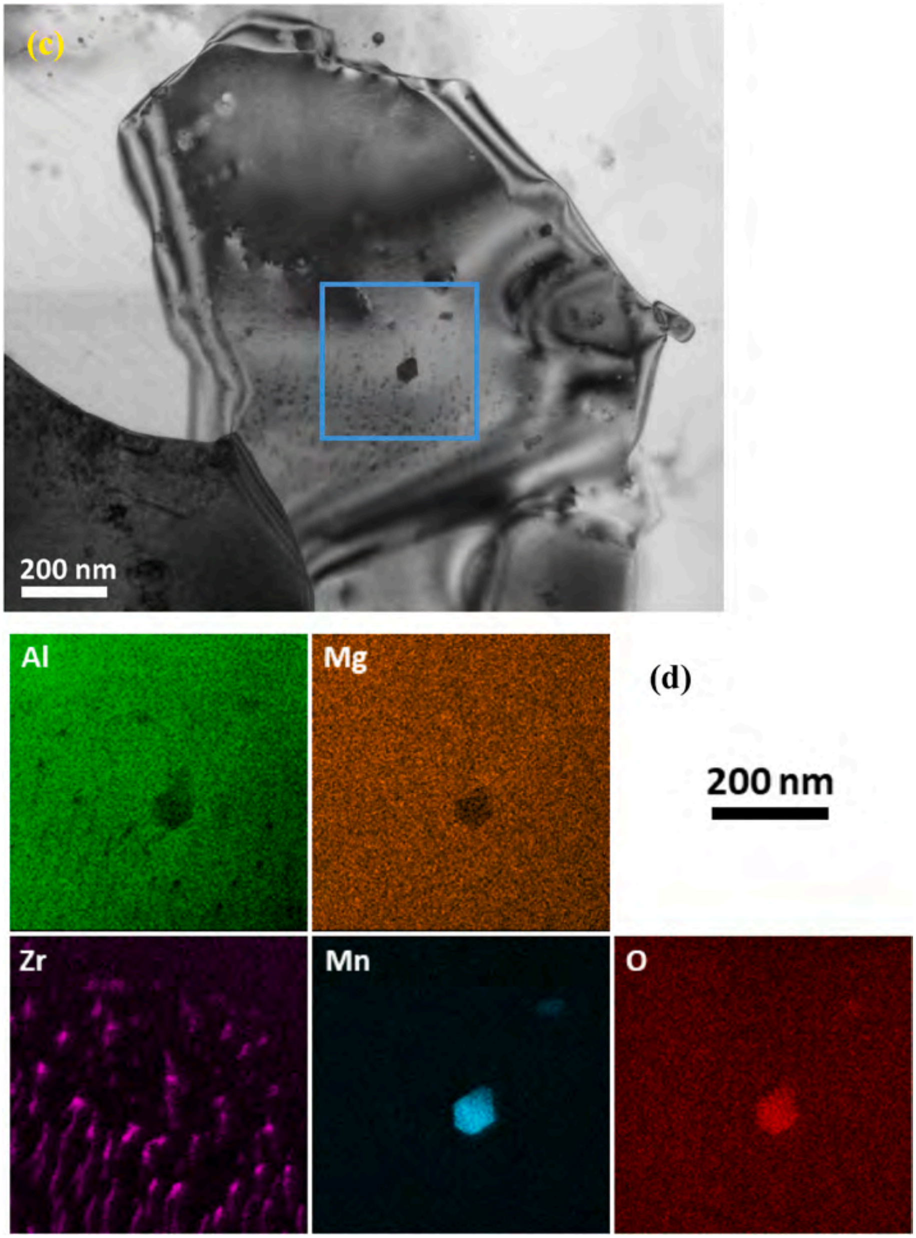

Fig. 6. (*continued*).

number of mobile dislocations, resulting from their absorption (sinking) at grain boundaries and potential pinning by Mg solute atoms [17]. The 0.2 % offset yield stress value, in particular, serves as a critical parameter for setting the stress levels in the subsequent ultrasonic fatigue tests, ensuring that the material is subjected to stresses relevant to its mechanical performance under cyclic loading conditions.

3.4. VHCF S-N data

The S-N data presented in Fig. 10 compares the VHCF behavior of the studied PBF-LB Al-Mg-Zr alloy (data shown with red square markers) with conventionally fabricated (extruded) Al-5083 with ultrafine grains (UFG) and coarse grains (CG) [33]. The data is shown in two formats: a log-log scale, which excludes the run-out data, and a semi-log scale inset, which includes the run-out data marked with arrows. The comparison of VHCF performance between the extruded Al-Mg alloy and the PBF-LB Al-Mg-Zr alloy reveals substantial differences in their fatigue behavior. Specifically, it underscores the impact of microstructure and manufacturing processes (and associated defects) on their fatigue strength and durability under prolonged cyclic loading. In the VHCF regime (beyond 10^7 cycles), the extruded Al-5083 UFG shows the highest fatigue resistance, sustaining around 10^7 cycles at a stress amplitude of over 150 MPa and extending up to approximately 10^9 cycles at around 120 MPa. Its fatigue strength in the VHCF domain stabilizes near 110 MPa, indicating excellent mechanical performance even under long-term cyclic loading. In contrast, extruded Al-5053 CG exhibits slightly lower fatigue performance, with a fatigue strength of about 100 MPa in the VHCF regime [33]. Despite this, the coarse-grained structure still shows considerable resilience, sustaining cyclic loads up to 10^9 cycles, though at reduced stress amplitudes compared to the ultrafine-grained variant.

The studied PBF-LB-processed Al-Mg-Zr alloy reveals the lowest fatigue strength in both high-cycle and VHCF regimes, sustaining stress amplitudes of around 120 MPa at 10^7 cycles, but decreasing to approximately 90 MPa at 10^9 cycles. This underperformance is mainly attributed to the presence of AM–induced defects, such as process-

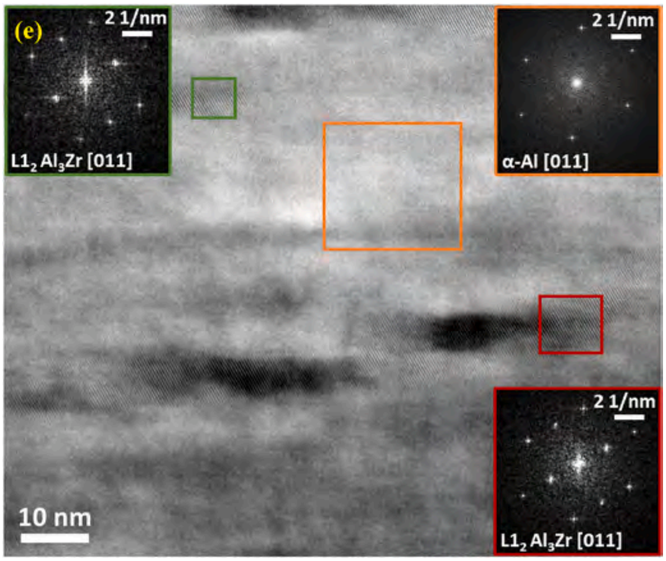

Fig. 6. (*continued*).

induced pores/lack of fusion and residual stresses, which act as crack initiation sites and accelerate VHCF failure under cyclic loading. Indeed, the largely dense structure of extruded alloys contributes significantly to their enhanced mechanical properties, allowing them to withstand higher stress amplitudes. This densification results in a more uniform microstructure, reducing the likelihood of defect-induced crack initiation. For example, Al-5083 UFG maintains its superior performance even beyond 10^9 cycles, underscoring its exceptional robustness under long-term fatigue conditions. This extended fatigue life can be attributed to the ultrafine grain structure, which enhances resistance to crack propagation and delays fatigue failure, making it an ideal candidate for applications requiring prolonged cyclic durability.

The S-N data on a log-log scale (excluding the runout data points) aligns well with the Basquin equation, which establishes a relationship between stress amplitude (σ_a), the fatigue strength coefficient ($\acute{\sigma_f}$), the number of cycles to failure (N_f), and the fatigue strength exponent (b) as in Eq. (1):

$$\sigma_a = \acute{\sigma_f} . N_f^b \qquad \text{Eq. 1}$$

For the extruded Al-5083 UFG (blue circles) [33], the Basquin equation $\sigma_a = 322.18N_f^{-0.030}$, with an acceptable R^2 of 0.70 and a good fatigue resistance in the VHCF regime. The flatter slope shows that this material retains its fatigue strength over time, though the moderate R^2 reflects some variability in the data. On the other hand, the extruded Al-5053 CG (green triangles) [33] follows a very flat slope, $\sigma_a = 179.95N_f^{-0.011}$, suggesting minimal loss in stress amplitude, meaning high resistance to fatigue degradation. However, the low R^2 of 0.30 indicates significant scatter and weak adherence to the Basquin model, reflecting variability due to the microstructure or testing conditions.

In contrast, the studied PBF-LB Sc-free Al-Mg-Zr alloy (red squares) shows the most pronounced reduction in fatigue strength with the steepest Basquin slope ($\sigma_a = 306.0157$) and a high R^2 of 0.90, suggesting a strong fit to the model. This steeper slope implies that the PBF-LB alloy experiences faster degradation in fatigue life when the stress amplitude is increased, compared to the extruded alloys, possibly due to the increase in stress intensity at the volumetric defects like lack of fusion, keyhole, and gas pores. The R^2 value of 0.90 for the PBF-LB alloy is noteworthy, especially given the inherent unpredictability in PBF-LB materials due to the variability in the size, shape, and distribution of pores. This adherence to the Basquin model can be attributed to repeatable and predictable fatigue failure mechanisms in the studied material. While the presence of PBF-LB-caused volumetric defects like lack of fusion and porosity often introduces variability in fatigue behavior, the strong fit observed here may result from consistent defect characteristics in the tested specimens. Additionally, the better correlation with the Basquin model highlights a key advantage: predictable failure behavior, which is preferable to less predictable performance, even if fatigue life is somewhat lower. This consistency in failure mechanisms reflects the optimized PBF-LB process used to fabricate the Sc-free Al-Mg-Zr alloy.

3.5. *Fractography analysis*

Fig. 11 presents the fractographic and elemental analysis of the fatigue failure origins in two PBF-LB Al-Mg-Zr specimens subjected to USF testing. The fractographic images, along with the corresponding elemental maps, provide insight into defect characteristics that contributed to crack initiation, which eventually led to failure under cyclic loading. In Fig. 11a, three SEM images progressively zoom in on the fatigue fracture surface of specimen F4, which failed at 98 MPa after 5.81×10^8 cycles. The sequence of images shows the overall fracture surface on the left, followed by a closer view of the crack initiation site in the center image, and finally, a highly magnified image on the right, focusing on the critical defect identified at the crack initiation site. The highlighted defect, with a size of approximately 83.08 μm, is located 27.16 μm away from the material's surface (this is the distance from the edge of the defect to the free surface of the specimen). This defect appears to have played a significant role in crack initiation due to its proximity to the surface and the stress concentration during cyclic loading. The magnified image on the right (Fig. 11a) presents the layered energy dispersive spectroscopy (EDS) map of the entire area, illustrating the distribution of individual elements and oxides (also shown at the bottom), along with the measured composition at two locations (marked by white rectangles #1 and #2). The defect in Fig. 11a exhibits two distinct features: (i) a tortuous, dark/hollow region corresponding to a lack of fusion (LoF) defect (i.e., a void) and (ii) a surrounding area composed of oxides, predominantly aluminum oxides with minor amounts of magnesium oxides, as determined by EDS analysis. Fig. 11b similarly presents the SEM fractography of specimen F5, which also failed at 98 MPa but after 6.30×10^8 cycles. The overall fracture surface (left) shows a circular crack initiation area, and the middle image zooms into this initiation site, revealing a larger defect compared to the one in specimen F4. This defect has a size of approximately 150.50 μm and is located 990.13 μm away from the surface (i.e., close to the center of the specimen). The defect in F5 is notably larger

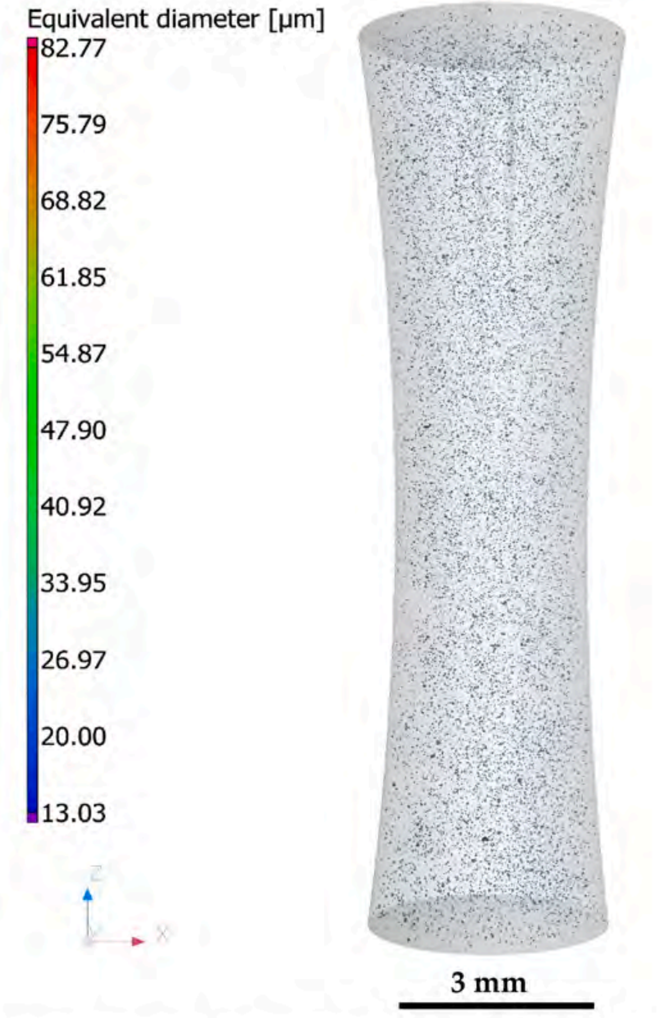

Relative Density	Max Defect Size	Average Defect Size
99.91%	82.77 μm	18.99 μm

(a)

Fig. 7. (a) 3D visualization of defect distribution within the gauge section of a fatigue coupon; (b) largest defect, found in the scanned volume, visualized in XY, YZ, and ZX orientation; (c) magnified view of defect distribution at a plane perpendicular to the applied stress direction (Z) at the minimum diameter; (d) bar chart representation of defect size distribution showing the frequency of defects across size ranges.

and consists of multiple clustered LoF voids and pores surrounded by a bright region of fine granular area (FGA). The right side of Fig. 11b reveals the intricate morphology of the defect by presenting the layered EDS map of the entire defect region, along with the measured composition from a specific location within the defect (marked with rectangle #3). The EDS analysis at location #3 revealed a significant oxygen concentration (13.30 %), indicating the presence of oxide inclusions, primarily aluminum oxides with some magnesium oxides, within the defect. This suggests that the clustered LoF voids and pores are embedded with oxides, which likely facilitated crack nucleation and played a critical role in fatigue failure. Therefore, defects play a critical role in fatigue crack initiation in PBF-LB Al-Mg-Zr alloys even at low stress levels like 98 MPa. The defect size and location, whether near the surface (as in specimen F4) or deeper within the material (as in specimen F5), considerably influence the fatigue performance of the material. The presence of clustered defects or oxides can exacerbate this by providing localized stress concentrations, leading to reduced fatigue life, especially when they are close to the surface.

Fig. 12 illustrates the influence of defect size and location on the fatigue life of the material tested at the same stress level of 107 MPa. The images highlight different fatigue crack initiation mechanisms, including surface, subsurface, and internal initiation, with variations in defect size and location contributing significantly to fatigue life. In Fig. 12a, specimen F7 shows crack initiation from a surface defect, with a measured defect size of ~74.66 μm and a defect length of 96.8 μm at the surface. This surface initiation resulted in a fatigue life of 2.41×10^{7} cycles. Surface defects are generally more detrimental to fatigue life, allowing cracks to initiate and propagate with minimal resistance. The EDS analysis (Spectrum 4) of the marked region within the defect site (right side of Fig. 12a) reveals an oxygen content of 1.84 %, indicating a relatively low degree of oxidation. The primary failure mechanism was likely driven by stress concentration at the defect site (i.e., an irregular void or LoF defect) rather than oxide-related embrittlement. Fig. 12b presents a subsurface defect in specimen F9, located ~10.12 μm away

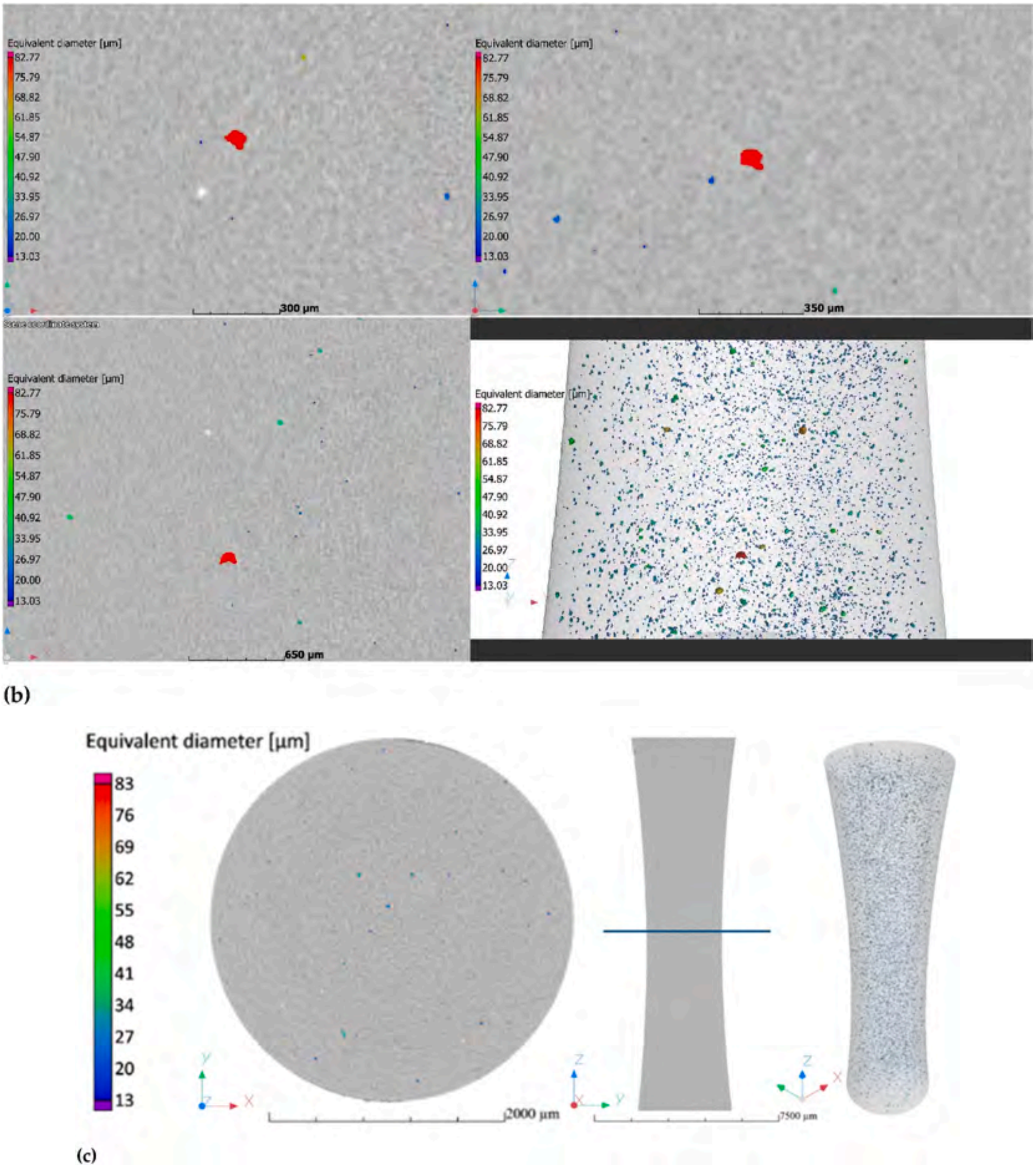

Fig. 7. (*continued*).

from the surface with a defect size of ~53.18 µm. This specimen exhibited a longer fatigue life of 1.14×10^8 cycles, likely due to the shielding effect of the surrounding material, which delayed crack propagation compared to the surface defects shown in Fig. 12a. Fig. 12b reveals two distinct defects, with crack initiation most likely originating from the upper defect. EDS composition analysis was conducted at two locations: (i) inside the LoF void (marked by a '+' sign), which showed no significant oxide presence, and (ii) at the bottom-right defect (marked by rectangular box 5), which exhibited substantial oxide accumulation (oxygen content: 29.83 %). The bottom-right defect is an irregularly shaped LoF, characterized by rough internal surfaces and surrounded by oxidation products. EDS analysis confirms the presence of aluminum oxides with minor MgO contributions, suggesting oxidation during processing or subsequent exposure. The defect's morphology, combined with localized oxidation, may have contributed to microstructural embrittlement, potentially accelerating crack propagation under cyclic loading. Fig. 12c shows internal crack initiation for specimen F10, characterized by a distinct "fisheye" fracture pattern. This internal defect, with a size of approximately 93.65 µm and located at a depth of 256.37 µm, consists of a cluster of pores surrounded by an FGA and oxide formation (EDS composition at the core of the defect shows an oxygen content of 22.70 %). These oxides are primarily aluminum oxides with slight MgO content. This microstructural feature distinguishes it from the LoF defects and isolated pores observed in Fig. 12a and b. The clustered defects in Fig. 12c, along with the FGA formation, indicate a prolonged fatigue crack initiation phase, as the granular zone suggests microstructural damage preceding crack propagation. The internal location of the defect buffers stress concentrations due to the surrounding intact material, significantly delaying crack growth and resulting in the longest fatigue life of 4.65×10^8 cycles. This fish-eye fracture pattern is a hallmark of VHCF regimes and highlights the role of defect morphology and location in determining fatigue life.

Fig. 13 presents the effects of defect size and location on the fatigue crack initiation mechanisms and overall fatigue life of the studied alloy, tested at a stress level of 117 MPa. Fig. 13 reveals various crack initiation sites and mechanisms, including multiple subsurface, single subsurface, and internal initiation, demonstrating how these factors influence fatigue life under cyclic loading. In Fig. 13a, specimen F11 exhibits multiple subsurface crack initiation sites, with two critical defects simultaneously contributing to fatigue failure at 3.83×10^6 cycles. The

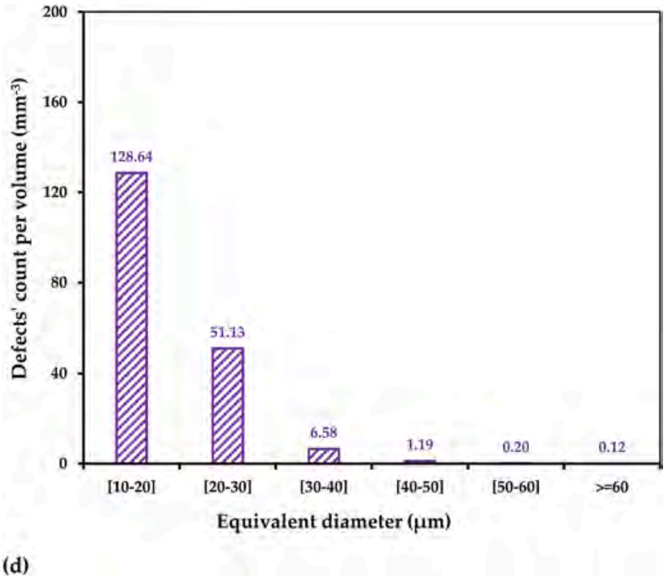

Fig. 7. (*continued*).

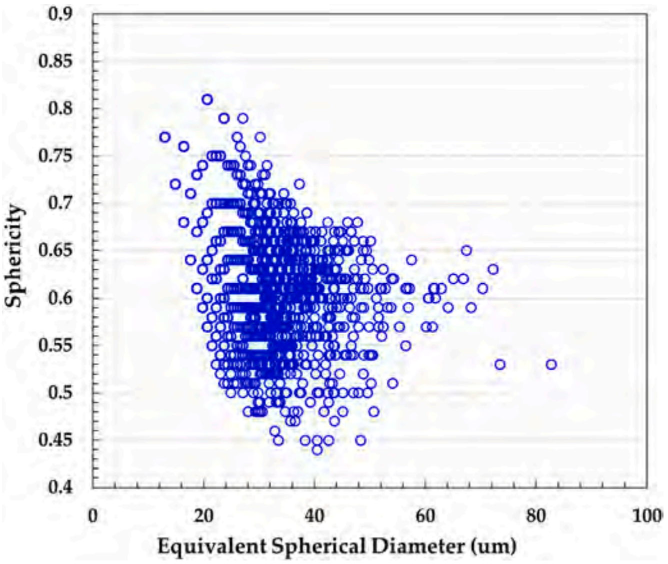

Fig. 8. Sphericity concerning defect Equivalent diameter.

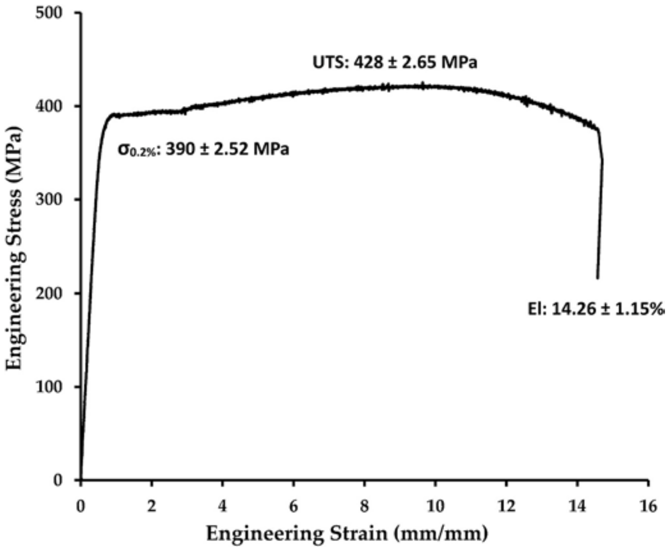

Fig. 9. Average flow curve Tensile behavior of the investigated PBF-LB Al-Mg-Zr in aged condition ($\sigma_{0.2\ \%}$: 0.2 % offset stress, UTS: ultimate tensile strength, El: elongation).

top defect measures 31.08 μm and is located 18.4 μm from the surface, while the bottom-right defect measures 38.8 μm and is positioned 14.14 μm away. EDS analysis at location #7 confirms a high oxygen concentration (12.30 % O), indicating oxide inclusions within the crack path, predominantly composed of Al oxides with minor Mg oxides. Similarly, location #8, within the spherical pore, contains 1.93 % O, suggesting a lower oxide presence compared to location #7. The oxygen map reveals a dispersed oxide distribution within the defect, while Mg and Zr maps indicate that these elements remain more uniformly distributed in the surrounding matrix. Fig. 13b shows a single subsurface defect in specimen F12, measuring 65.5 μm in size and located 4.87 μm below the surface. This configuration results in a fatigue life of 8.48×10^6 cycles, longer than the specimen with multiple initiation sites. The layered EDS map along with composition from specific locations (10&11) and distribution of Al, Mg, Zr, and O are presented similarly. Fig. 13c illustrates an internal initiation with the "fisheye" pattern again in specimen F13. This defect is measured 152.3 μm in size and is located deeply within the material at a depth of 1097.34 μm from the surface. The isolated internal defect and its distance from the surface contribute to a significantly longer fatigue life of 2.84×10^7 cycles, as the internal location prevents direct exposure to external cyclic stresses. The corresponding elemental analysis shows a relatively lower presence of the oxide particles in this case.

The fisheye pattern is a characteristic crack initiation mechanism of VHCF where cracks initiate and grow within the material's interior before reaching the surface. Internal defects require higher stress cycles to propagate to failure, thus resulting in enhanced fatigue life. Therefore, Figs. 12 and 13 highlight experimental evidence and show that defect size and location are critical in determining the fatigue life of PBF-LB alloys. Larger defects located closer to the surface result in shorter fatigue lives, while deeply embedded internal defects significantly extend the fatigue life. In this study, all specimens that failed within the 10^8-cycle range exhibited crack initiation from within the specimen, whereas stress levels above 137 MPa (35 % of the YS) generally led to surface-initiated cracks.

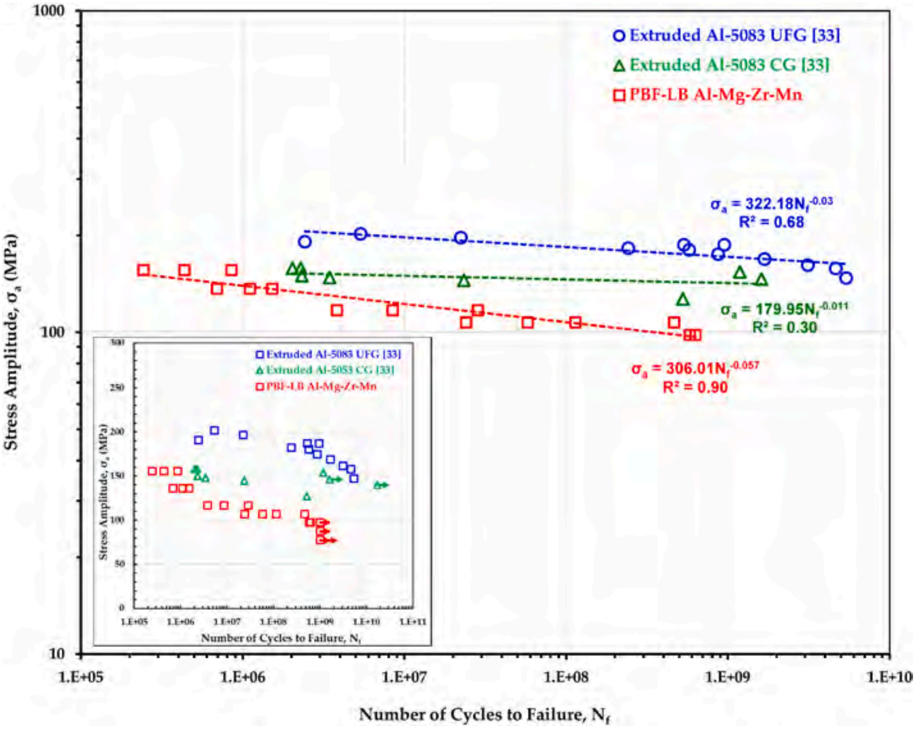

Fig. 10. Basquin fit of the VHCF S-N data in a log-log coordinate system, excluding the runouts, of the studied PBF-LB Al-Mg-Zr alloy in comparison with extruded UFG and CG Al-5083 reported by Meng et al. [33]; the insert shows the S-N data including the runouts on a semi-log coordinate system.

The fractographic observations are summarized in Table 2, detailing the defect measurements in VHCF-failed specimens, including stress amplitude, fatigue life, size of the critical defect, distance from the surface to the edge/boundary of the defect, defect length at the surface (i.e., the free length of the defect exposed at surface) and the type of defect (e.g., LoF, gas pores, oxides). Specimens F1 through F6, which withstood stress amplitudes of 78–98 MPa, achieved the highest fatigue lives, with several reaching 10^9 cycles (i.e., runout). As stress amplitude increased, from 107 MPa to 156 MPa, the fatigue life decreased significantly, and critical defects were observed more frequently in action and their variation in size and location was found to be significantly correlated with fatigue performance, as discussed throughout the fractography section.

For specimens tested at 107 MPa, fatigue life ranged from 2.41×10^7 to 4.65×10^8 cycles, with critical defect sizes ranging from 53.18 μm to 130.21 μm. Higher stress amplitudes, such as 117 MPa, show a reduction in fatigue life, ranging between 3.83×10^6 and 2.84×10^7 cycles, with critical defect sizes increasing up to 152.3 μm, located internally or at the surface. For the stress amplitudes of 137 and 156 MPa, crack initiation was predominantly observed at the surface, with defect lengths of up to 42.04 μm and 41.68 μm, respectively, and fatigue lives under 10^6 cycles. Therefore, Table 2 highlights the correlation between stress amplitude, defect location, and defect size with the resulting fatigue life, illustrating that larger subsurface or internal defects are less detrimental and contribute to extended fatigue life compared to surface defects causing high-stress concentrations that lead to shorter fatigue life.

Based on the fractography measurements summarized in Table 2, the most critical defects identified in VHCF-failed specimens ranged in size from 30 to 80 μm. Three larger defects, exceeding 100 μm, were observed at the center of fish-eye fracture patterns. These larger defects differed in composition, consisting of lack-of-fusion voids surrounded by oxides or fine granular regions, which collectively contributed to crack initiation (see Fig. 11b, 12c and 13c). Notably, these defects were not analogous to those detected via XCT. Unlike these complex defects, XCT primarily captured voids, providing a different perspective on defect characterization. The XCT analysis revealed defect sizes ranging from 13 to 83 μm, with the majority below 30 μm. Excluding the three outliers (based on size and nature) identified in fractography, the defect size distribution from XCT closely aligned with the critical defect sizes observed in VHCF-failed specimens. Additionally, XCT identified numerous smaller defects (<30 μm), which were not found to significantly impact fatigue life, as corroborated by fractographic analysis. These findings emphasize the critical role of defects within the 30–80 μm range in fatigue crack initiation and underscore the necessity of minimizing larger defects during the PBF-LB process to enhance fatigue performance in VHCF regimes.

3.6. *Fracture mechanics modeling and fatigue life predictions in the presence of defects*

The stress intensity factor (SIF) provides important indications of the crack driving force and is dependent on the applied stress amplitude and the crack size. It can be calculated employing Eq. (2) [50–53].

$$\Delta K = A\,\sigma_a \sqrt{\pi \sqrt{\mathrm{area}_{\mathrm{defect}}}} \qquad \text{Eq. 2}$$

where A is a dimensionless constant accounting for the defect location influence and that takes a value of 0.5 for internal defects and 0.65 for surface/subsurface defects [54]. The crack size is measured as the square root of the defect area measured on a plane perpendicular to the direction of the maximum stress axis [54].

Fig. 14 illustrates the fracture morphology and corresponding SIF analysis for PBF-LB Al-Mg-Zr alloy specimens, emphasizing the influence of defect location on crack initiation. In Fig. 14a, the fracture surfaces mark distinct regions, starting with a crack-initiating defect, which can be located at the surface/subsurface, or internally within the material. For internal defects, the fracture morphology exhibits a characteristic fish-eye pattern. The fish-eye pattern includes the internal initiation at a defect/inclusion/microstructural inhomogeneity, followed by relatively unstable propagation, with the associated fracture surface area being rough, continuing up to the fish-eye border, which marks the end of crack propagation under cyclic loading. This is

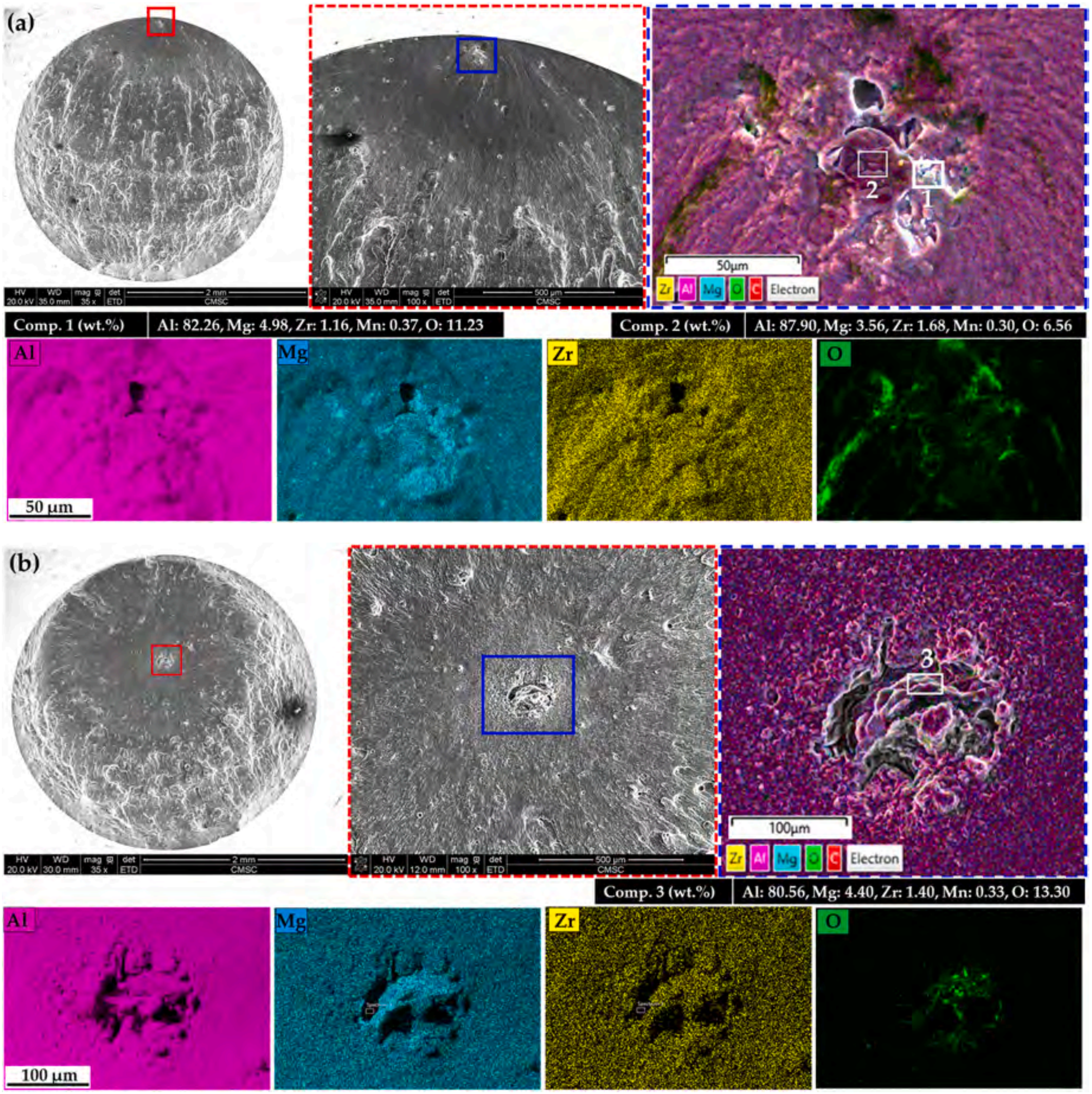

Fig. 11. (a) SEM images of specimen F4 (98 MPa, 5.81×10^8 cycles) showing a defect size of 83.08 μm at 27.16 μm from the surface. (b) SEM images of specimen F5 (98 MPa, 6.30×10^8 cycles) with a larger defect size of 150.50 μm at 990.13 μm from the surface. Corresponding EDS elemental maps reveal the distribution of Al, Mg, Zr, and O around the defects, indicating potential oxide formation.

followed by the final fracture zone, where rapid fracture occurs as the crack reaches critical size and exceeds the material fracture toughness. This fish-eye pattern is notably different from regular fracture morphologies typically observed in conventional fatigue, where a critical defect at or near the surface leads to a stable crack propagation zone (CPZ) and eventual failure without the distinct features of fish-eye zones. These distinct regions on the fracture surface can be directly related to SIF, which varies across different propagation zones. However, the SIFs associated with the initial defect, or the FGA are important for the VHCF fatigue response, since most of the VHCF life is consumed in the crack initiation process and this stage must be considered for the design.

Fig. 14b displays the variation in the SIF (ΔK) associated with the initial defect as a function of the square root of the defect area for different defect locations. The SIF values (ΔK) are categorized by location of initiation: surface, subsurface, and internal. Interestingly, as discussed throughout the fractography section (Figs. 11–13), this analysis confirms that surface and subsurface defects are smaller than the internal defects that initiated fatigue cracks. Indeed, for the same applied stress amplitude, defects should be larger to originate a fatigue failure if located internally. The initiation site involved the combination of process-induced pores/LoFs, inclusion (e.g., oxide formation shown in Fig. 11b), and microstructural inhomogeneity that makes the defect size for internal initiation or fisheye fracture relatively larger. SIF is averagely constant, with limited variations among the three groups considered and without a clear increasing or decreasing trend. Overall, the average SIF values calculated for initiation sites, either surface or internal, is close to 1 MPa$\sqrt{}$m.

Fig. 14c displays the variation in the SIF (ΔK) associated with the initial defect as a function of the number of cycles to failure. Even if the fatigue life is considered, the trend of SIF is almost constant and flat. This trend is in agreement with literature data on VHCF failures obtained by considering the FGA size [55] and can be explained by considering that the crack initiation stage takes place in a small region around the initial defect, with the possible formation of an FGA very close to it. For example, for specimen F5 (Fig. 11) an FGA close to the initial defect has

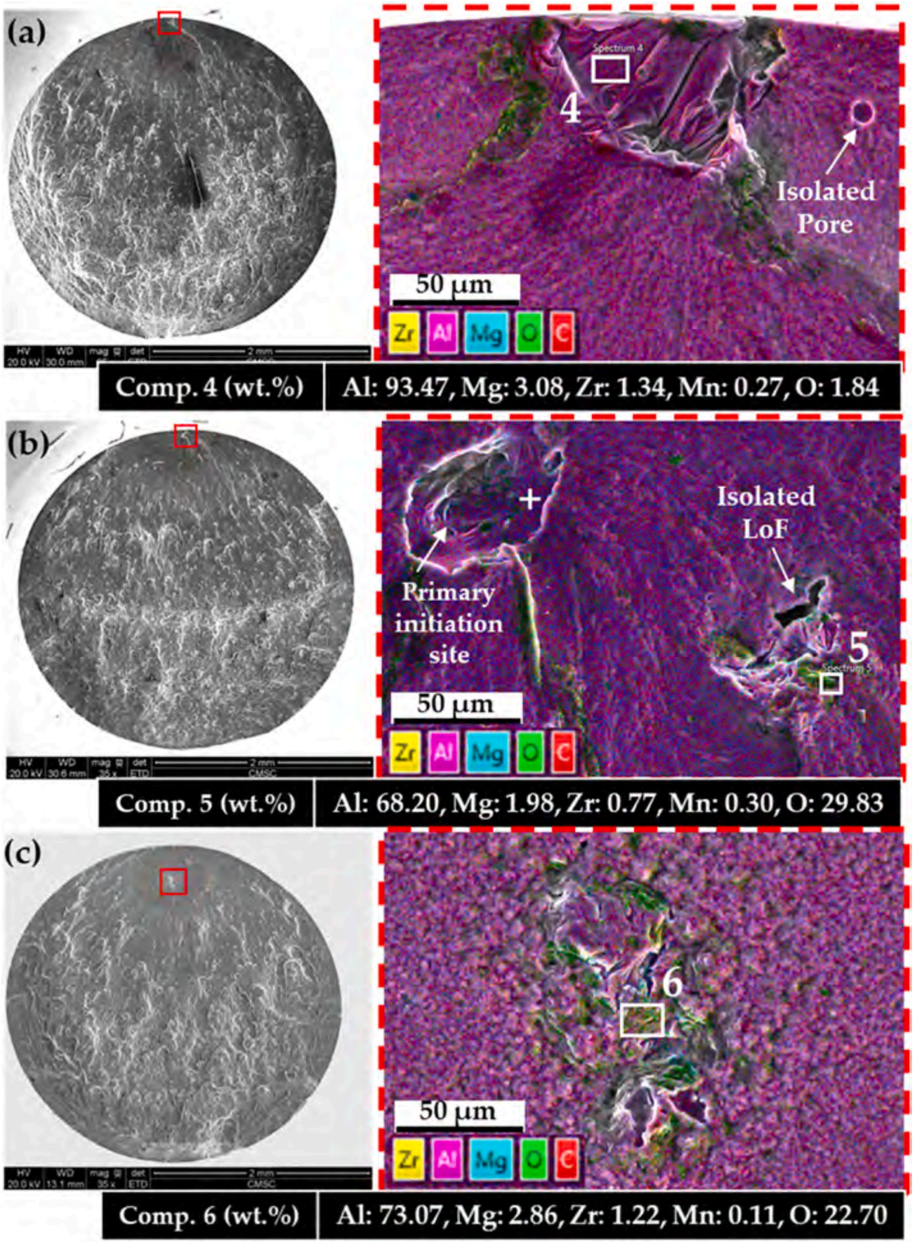

Fig. 12. Display of different initiation mechanisms at the same stress level of 107 MPa: (a) Initiation from the surface for Specimen F7 (2.41×10^7 cycles) with a defect size of 74.66 µm and a defect length of 96.8 µm at the surface; (b) Subsurface defect for Specimen F9 (1.14×10^8 cycles) displaying a defect size of 53.18 µm located 10.12 µm from the surface; (c) Internal initiation with characteristic fish-eye formation for Specimen F10 (4.65×10^8 cycles) exhibiting a defect size of 93.65 µm at a depth of 256.37 µm.

been found, but it can be hardly distinguished from the initial defect. The boundary between the initial defect and the FGA is not easily identifiable, with the measured defect size potentially including this peculiar area with fine grains. This is the reason for the flat trend found in Fig. 14c and for the large experimental scatter. Moreover, this analysis also confirms that the area very close to the defects and with a rough texture is responsible for the crack initiation, with the regions outside this region involved in the subsequent crack propagation. Accordingly, the SIF for the initial defect can be conservatively assumed as the SIF threshold, and being constant, large defects can be those showing the largest fatigue life if subjected to low-stress amplitudes.

3.6.1. *Fatigue life modelling*

Reliable models for fatigue life prediction must consider the characteristic defect size. In general, the defect population or the largest defect expected within a part to be designed should be a fundamental input to be considered for the fatigue response modeling and can be obtained, for example, with XCT inspections and/or by exploiting the properties of the Largest Extreme Value Distribution (LEVD). Several models have been proposed in the literature to model this dependency and most of them are based on the integration of the Paris law, especially for investigating the VHCF life region [56]. However, despite its effectiveness, this approach requires the estimation of many unknown constants, to model the crack propagation between the initial defect and the FGA border and between the FGA border and the Fish-eye limits. These constant coefficients are generally assumed or estimated since they can be hardly estimated experimentally, or specific experimental procedures are not available. Moreover, these models generally are deterministic and do not consider the intrinsic statistical scatter associated with the fatigue phenomenon [56], which is instead crucial for a safe design,

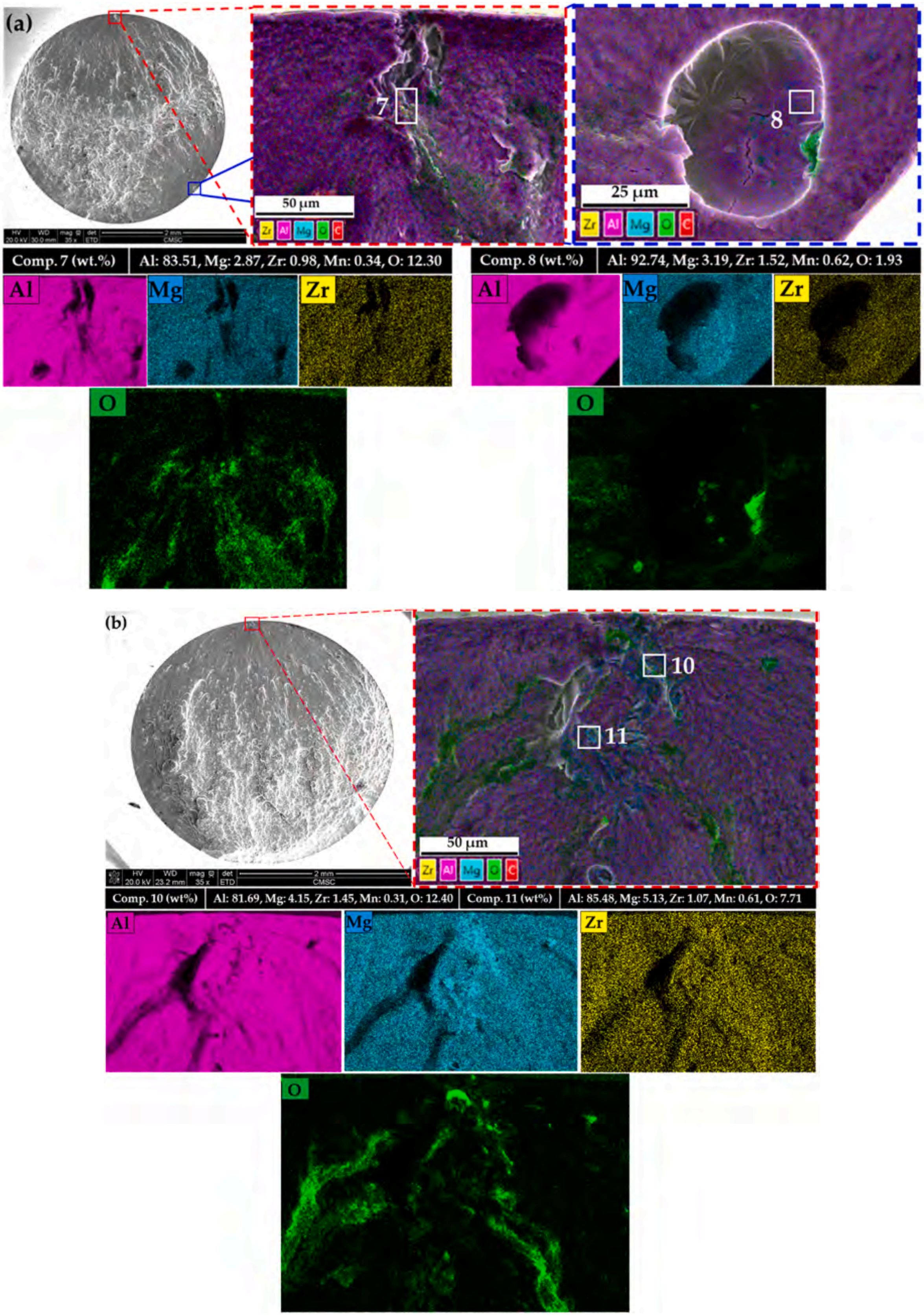

Fig. 13. Variation in initiation mechanisms at the same stress level of 117 MPa: (a) Multiple subsurface initiation for F11 (3.83×10^6 cycles) with a defect size of 31.08 μm, 18.4 μm away from the top surface and defect size of 38.8 μm, 14.14 μm away from the bottom-right surface; (b) Subsurface defect for F12 (8.48×10^6 cycles) with defect size of 65.5 μm, 4.87 μm away from surface; (c) Internal initiation with fish-eye pattern for F13 (2.84×10^7 cycles) exhibiting a defect size of 152.3 μm, distance from surface is 1097.34 μm.

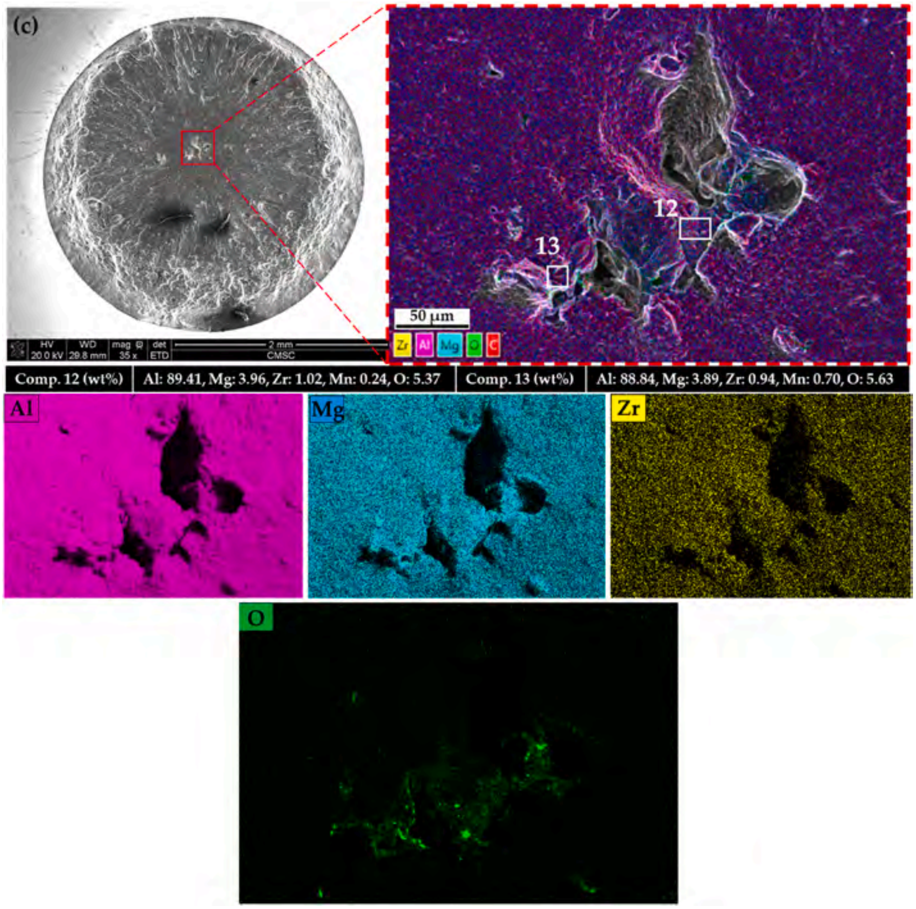

Fig. 13. (*continued*).

Table 2
Summary of fractography-based defect measurement on VHCF failed specimens.

ID	Stress amplitude (MPa)	Number of cycles (N_f)	Largest/critical defect Size (µm)	Distance from the surface (µm)	Defect length at the surface (µm)	Defect Type
F1	78	>1.00E+09	–	–	–	–
F2	78	>1.00E+09	–	–	–	–
F3	88	>1.00E+09	–	–	–	–
F4	98	5.81E+08	83.08	27.16	0	LoF + Al_2O_3+MgO
F5	98	6.30E+08	150.50	990.13	0	LoF + Al_2O_3+MgO + FGA
F6	98	>1.00E+09	–	–	–	–
F7	107	2.41E+07	74.66	0	96.80	LoF
F8	107	5.78E+07	56.36	0	16.30	LoF
F9	107	1.14E+08	53.18	10.12	0	LoF
F10	107	4.65E+08	130.21	256.37	0	LoF + Al_2O_3+MgO + FGA
F11	117	3.83E+06	31.08	18.40	0	LoF + Al_2O_3+MgO
F11	117	3.83E+06	38.80	14.14	0	Gas Pore
F12	117	8.48E+06	65.50	4.87	0	LoF + Al_2O_3+MgO
F13	117	2.84E+07	152.30	1097.34	0	LoF + Al_2O_3+MgO + FGA
F14	137	6.92E+05	31.97	0	42.04	LoF
F15	137	1.11E+06	34.09	0	30.05	LoF
F16	137	1.52E+06	33.27	0	8.05	LoF + Al_2O_3+MgO
F17	156	2.44E+05	37.73	0	41.68	LoF
F18	156	4.36E+05	26.59	0	40.25	LoF
F19	156	8.52E+05	48.23	21.49	0	LoF + Al_2O_3+MgO

especially if the crack originates from defects. To overcome these issues, in this work the relationship between the fatigue life, the applied stress amplitude, and the defect size is modeled with the "marginal P-S-N curves" model developed by the authors. In particular, the cumulative distribution function, $F_Y(y;x)$, of the logarithm of the fatigue life, $y = \log_{10}(N_f)$, can be expressed with the formula reported in Eq. (3):

$$F_Y(y;x) = \int_0^\infty F_{Y|\sqrt{Area}}(y;x,\sqrt{area})f_{\sqrt{Area}}(\sqrt{area}) \bullet d\sqrt{area}, \qquad \text{Eq. 3}$$

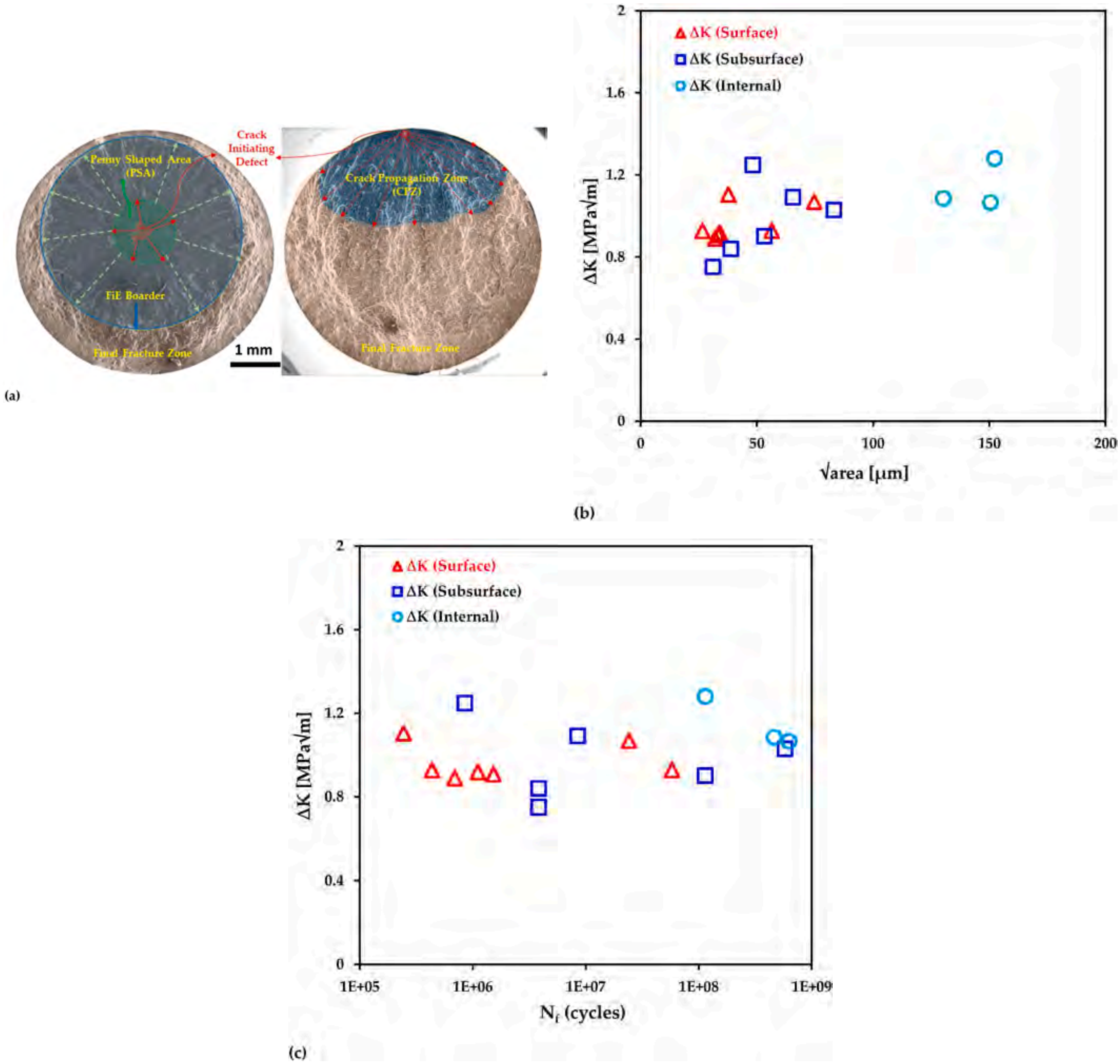

Fig. 14. (a) Distinct initiation and propagation zones associated with internal and surface/sub-surface initiation, and (b, c) SIF range (ΔK) analysis, illustrating its variation with defect size and number of cycles, respectively, for PBF-LB Al-Mg-Zr alloy specimens tested in the HCF to VHCF domain.

being $x = \log_{10}(s_a)$, s_a the applied stress amplitude, $f_{\sqrt{area}}(\sqrt{area})$ the probability density function of the defect size random variable $\sqrt{Area}$, assumed to follow a LEVD. $F_{Y|\sqrt{Area}}(y; x, \sqrt{area})$ is the cumulative distribution of the conditional fatigue life, with the logarithm of the fatigue life random variable Y (the capital letter is used for the random variable) assumed to be normally distributed, with constant standard deviation and the mean that linearly decreases with x and the logarithm of the characteristic defect size $\sqrt{area}$. According to Eq. (3), the conditional fatigue life, dependent on the applied stress amplitude and on $\sqrt{area}$, is marginalized and averaged on the distribution of the defect size, therefore considering not only a specific defect size but the distribution of the critical defect sizes, i.e., those controlling the fatigue response. According to this procedure, there is no need to assume the constant coefficients involved in the different stages of crack nucleation and propagation, and the coefficients present in the model are estimated from the available data on the applied stress amplitude, number of cycles to failure, and defect size. It is worth noting that an asymptotic trend, i.e., a VHCF fatigue limit, has not been considered, since the data show a monotonic decreasing trend even in the VHCF life range.

Fig. 15 plots the $\sqrt{area}$ of the defects originating the fatigue failures in a Gumbel plot, together with the estimated LEVD function. The constant coefficients are estimated with the least square method. Fig. 15b plots the marginal P-S-N curves on an S-N plot, with the experimental data. The median, the 0.1-th, and the 0.9-th quantile P-S-N curves are plotted. The parameter estimation has been carried out by applying the Maximum Likelihood Principle.

According to Fig. 15a, the LEVD is in good agreement with the experimental defects. The linear fitting on the Gumbel plot properly describes the experimental trend for defects with size above 40 μm. On the other hand, below 40 μm, the data seems to show an asymptotic

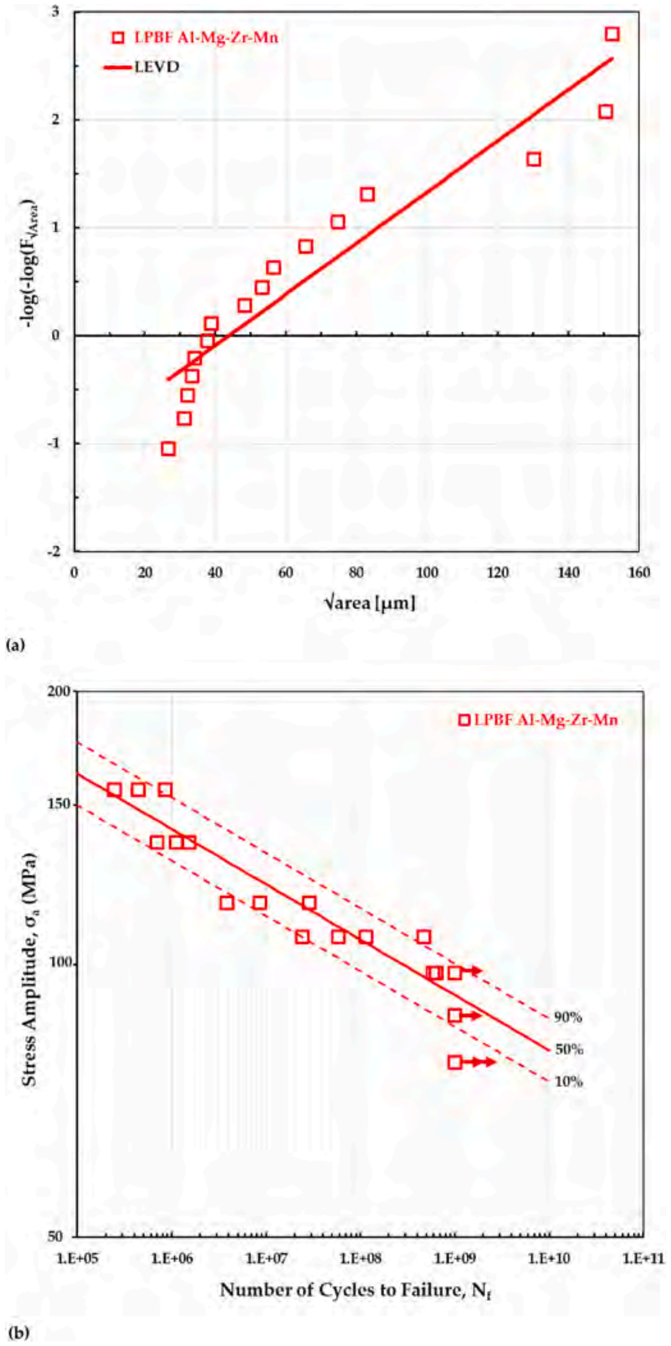

Fig. 15. Defect size distribution and P-S-N curves: (a) Gumbel plot of the defects originating the fatigue failures, and (b) Marginal P-S-N curves.

trend, with defects aligned vertically. However, more data is necessary to confirm an asymptotic trend.

Starting from the parameters for the LEVD, the marginal P-S-N curves have been estimated, and they are in good agreement with the experimental data. About 75 % of the data are within the interval between the 0.1-th and the 0.9-th P-S-N curves and the median P-S-N curve almost equally subdivides the experimental failures.

The results of this study highlight the inherent challenges associated with achieving defect-free components in PBF-LB-fabricated parts. In this work, defects, including pores, were found to contribute to fatigue failure in VHCF testing. At higher stress amplitudes, surface or near-surface defects acted as the dominant fatigue crack initiation sites, while at lower stress amplitudes, internal defects, and subsurface LoF/pores became more significant. These findings are consistent with established VHCF literature, where surface defects dominate crack initiation at higher stress levels, and internal defects are critical at lower stress levels. The stochastic nature of the PBF-LB process introduces variability in defect formation, driven by factors such as powder properties, laser stability, humidity conditions, and powder batches. While densities exceeding 99.9 % are achievable, eliminating all porosity in as-built components remains impractical. Many of the small, spherical pores observed in this study were gas atomization (GA) pores, inherent to the powder production process, which cannot be fully eliminated during printing. To address these limitations, process optimization strategies, such as using PREP (Plasma Rotating Electrode Processed) powder to reduce GA pores or incorporating remelting steps during PBF-LB fabrication, can significantly improve part quality. Additionally, post-processing methods, such as hot isostatic pressing (HIP), offer a viable approach to further reduce porosity and improve mechanical properties, particularly in fatigue-critical applications. Recognizing and mitigating these limitations are essential to advancing PBF-LB as a reliable manufacturing technology for high-performance applications.

4. Conclusions

The very high cycle fatigue (VHCF) performance of the PBF-LB Al-Mg-Zr alloy (EOS Al5X1) reveals crucial insights into the influence of process-induced defects on fatigue behavior. Despite the alloy's high relative density, even minor defects play a significant role in limiting its fatigue life, emphasizing the challenges and opportunities for optimizing additive manufacturing processes to enhance durability in cyclic-loading applications. Key findings from this study are summarized as follows.

i. The microstructure of the PBF-LB Al-Mg-Zr alloy (EOS Al5X1) consisted of a bimodal grain arrangement: a texture-free FGZ with equiaxed grains (<2 µm) near melt pool boundaries and a weakly textured CGZ transitioning to columnar morphology (~5 µm) at the melt pool core. KAM analysis showed relatively low local misorientations, while TEM revealed a high density of coherent Al_3Zr precipitates with an $L1_2$ structure, which refined grains, restrained boundary motion, and reinforced overall microstructural stability.
ii. The VHCF behavior of the alloy was primarily influenced by process-induced defects, such as pores and incomplete fusion, which significantly compromised the material's structural integrity under cyclic loading, leading to a fatigue strength of ~90 MPa at 1 billion cycles.
iii. Despite a high relative density of 99.91 %, microstructural analysis and XCT scans revealed that defects larger than 50 µm were sufficient to initiate fatigue cracks, confirming that even small defects play a critical role in VHCF crack initiation.
iv. The fractography analyses demonstrated both internal, subsurface, and surface crack initiation, with fish-eye patterns forming around internal cracks and larger defects at or near the surface driving surface crack initiation, highlighting the importance of defect size and location on fatigue life variability.
v. The fracture mechanics analysis highlights that under low-stress levels, the Stress Intensity Factor (SIF) computed by considering surface and internal defects is almost constant, with a flat trend concerning the defect size and the number of cycles to failures. The crack initiation process occurs in a very small region close to the defect, with the defect SIF which can be conservatively assumed as the SIF threshold and close to 1 MPa$\sqrt{m}$. A model for the prediction of the S-N curves which considers also the defect size influence has been employed, showing a good agreement with the experimental failures.

CRediT authorship contribution statement

Shawkat I. Shakil: Writing – original draft, Methodology, Formal analysis. **Wiktor Bednarczyk:** Writing – review & editing, Software, Resources, Formal analysis, Data curation. **Marta Gajewska:** Writing – review & editing, Software, Methodology, Investigation, Formal analysis, Data curation. **Zaynab Mahbooba:** Writing – review & editing, Validation, Resources. **Ankit Saharan:** Writing – review & editing, Resources, Project administration. **Andrea Tridello:** Writing – review & editing, Validation, Software, Methodology, Formal analysis. **Davide S. Paolino:** Writing – review & editing, Validation, Resources, Methodology. **Meysam Haghshenas:** Writing – review & editing, Supervision, Resources, Project administration, Funding acquisition, Conceptualization.

Declaration of competing interest

The authors declare that they have no known competing financial interests or personal relationships that could have appeared to influence the work reported in this paper.

Data availability

Data will be made available on request.

References

[1] C. Bathias, P.C. Paris, Gigacycle Fatigue in Mechanical Practice, CRC Press, 2004.
[2] L. Xu, Q. Wang, M. Zhou, Micro-crack initiation and propagation in a high strength aluminum alloy during very high cycle fatigue, Mater. Sci. Eng., A 715 (2018) 404–413.
[3] D.A. Celli, O. Scott-Emuakpor, J. Warner, T. George, Investigation of self-heating during ultrasonic fatigue testing and effect on very high cycle fatigue behavior of titanium 6Al-4V, J. Eng. Gas Turbines Power 145 (3) (2023) 031016.
[4] Bathias, There is no infinite fatigue life in metallic materials, Fatig. Fract. Eng. Mater. Struct. 22 (7) (1999) 559–565.
[5] R. Caivano, A. Tridello, G. Chiandussi, G. Qian, D. Paolino, F. Berto, Very high cycle fatigue (VHCF) response of additively manufactured materials: a review, Fatig. Fract. Eng. Mater. Struct. 44 (11) (2021) 2919–2943.
[6] X. Pan, L. Du, G. Qian, Y. Hong, Microstructure features induced by fatigue crack initiation up to very-high-cycle regime for an additively manufactured aluminium alloy, J. Mater. Sci. Technol. 173 (2024) 247–260.
[7] L. Liu, S. Wang, G. Li, Y. Ma, Microstructure study on very high cycle fatigue of an additively manufactured aluminium alloy via advanced characterization methods, Appl. Sci. 14 (5) (2024) 2025.
[8] S. Dixit, S. Liu, Laser additive manufacturing of high-strength aluminum alloys: challenges and strategies, Journal of Manufacturing and Materials Processing 6 (6) (2022) 156.
[9] J.H. Martin, B.D. Yahata, J.M. Hundley, J.A. Mayer, T.A. Schaedler, T.M. Pollock, 3D printing of high-strength aluminium alloys, Nature 549 (7672) (2017) 365–369.
[10] T. DebRoy, H.L. Wei, J.S. Zuback, T. Mukherjee, J.W. Elmer, J.O. Milewski, A. M. Beese, A. Wilson-Heid, A. De, W. Zhang, Additive manufacturing of metallic components – process, structure and properties, Prog. Mater. Sci. 92 (2018) 112–224.
[11] Y. Cao, H.L. Wei, T. Yang, T.T. Liu, W.H. Liao, Printability assessment with porosity and solidification cracking susceptibilities for a high strength aluminum alloy during laser powder bed fusion, Addit. Manuf. 46 (2021) 102103.
[12] D. Schimbäck, P. Mair, M. Bärtl, F. Palm, G. Leichtfried, S. Mayer, P.J. Uggowitzer, S. Pogatscher, Alloy design strategy for microstructural-tailored scandium-modified aluminium alloys for additive manufacturing, Scr. Mater. 207 (2022) 114277.
[13] S.I. Shakil, L. González-Rovira, L. Cabrera-Correa, J. de Dios López-Castro, M. Castillo-Rodríguez, F.J. Botana, M. Haghshenas, Insights into laser powder bed fused Scalmalloy®: investigating the correlation between micromechanical and macroscale properties, J. Mater. Res. Technol. 25 (2023) 4409–4424.
[14] T. Dorin, M. Ramajayam, A. Vahid, T. Langan, Chapter 12 - aluminium scandium alloys, in: Lumley (Ed.), Fundamentals of Aluminium Metallurgy, Woodhead Publishing2018, 439-494.
[15] T.J. Langan, T. Dorin, Scandium in commercial wrought aluminum alloys. Rare Earth Metals and Minerals Industries: Status and Prospects, 2023, pp. 359–389.
[16] J. Röyset, N. Ryum, Scandium in aluminium alloys, Int. Mater. Rev. 50 (1) (2005) 19–44.
[17] R. Xu, R. Li, T. Yuan, H. Zhu, M. Wang, J. Li, W. Zhang, P. Cao, Laser powder bed fusion of Al–Mg–Zr alloy: microstructure, mechanical properties and dynamic precipitation, Mater. Sci. Eng., A 859 (2022) 144181.
[18] S. Griffiths, J.R. Croteau, M.D. Rossell, R. Erni, A. De Luca, N.Q. Vo, D.C. Dunand, C. Leinenbach, Coarsening-and creep resistance of precipitation-strengthened Al–Mg–Zr alloys processed by selective laser melting, Acta Mater. 188 (2020) 192–202.
[19] S. Griffiths, M.D. Rossell, J. Croteau, N.Q. Vo, D.C. Dunand, C. Leinenbach, Effect of laser rescanning on the grain microstructure of a selective laser melted Al-Mg-Zr alloy, Mater. Char. 143 (2018) 34–42.
[20] J.R. Croteau, S. Griffiths, M.D. Rossell, C. Leinenbach, C. Kenel, V. Jansen, D. N. Seidman, D.C. Dunand, N.Q. Vo, Microstructure and mechanical properties of Al-Mg-Zr alloys processed by selective laser melting, Acta Mater. 153 (2018) 35–44.
[21] S. Karna, L. Yuan, T. Zhang, R. Al-Aridi, A.J. Gross, D. Morrall, T. Krentz, D. Hitchcock, Microstructural analysis and defect characterization of additively manufactured AA6061 aluminum alloy via laser powder bed fusion, J. Mater. Sci. Technol. 219 (2025) 288–306.
[22] H. Liu, D. Gu, S. Keyu, H. Zhang, L. Li, Y. Zhang, J. Li, J. Qi, High-strength aluminum alloy processed by micro laser powder bed fusion (μ-LPBF): coordination of laser formability, microstructure evolution, and mechanical properties, J. Mater. Process. Technol. (2024) 118580.
[23] G. Li, X. Li, C. Guo, Y. Zhou, Q. Tan, W. Qu, X. Li, X. Hu, M.-X. Zhang, Q. Zhu, Investigation into the effect of energy density on densification, surface roughness and loss of alloying elements of 7075 aluminium alloy processed by laser powder bed fusion, Opt Laser. Technol. 147 (2022) 107621.
[24] Z. Wu, S. Wu, J. Bao, W. Qian, S. Karabal, W. Sun, P.J. Withers, The effect of defect population on the anisotropic fatigue resistance of AlSi10Mg alloy fabricated by laser powder bed fusion, Int. J. Fatig. 151 (2021) 106317.
[25] J. Li, J. Sun, G. Qian, L. Shi, Defect-induced cracking and fine granular characteristics in very-high-cycle fatigue of laser powder bed fusion AlSi10Mg alloy, Int. J. Fatig. 158 (2022) 106770.
[26] A. Mehta, L. Zhou, T. Huynh, S. Park, H. Hyer, S. Song, Y. Bai, D.D. Imholte, N. E. Woolstenhulme, D.M. Wachs, Additive manufacturing and mechanical properties of the dense and crack free Zr-modified aluminum alloy 6061 fabricated by the laser-powder bed fusion, Addit. Manuf. 41 (2021) 101966.
[27] S.I. Shakil, W. Bednarczyk, M. Gajewska, Z. Mahbooba, A. Saharan, A. Tridello, D. S. Paolino, M. Haghshenas, Fatigue characteristics of a newly developed laser powder bed fused scandium-free Al-Mg-Zr-Mn alloy, Int. J. Fatig. 193 (2025) 108738.
[28] P.D. Nezhadfar, S. Thompson, A. Saharan, N. Phan, N. Shamsaei, Structural integrity of additively manufactured aluminum alloys: effects of build orientation on microstructure, porosity, and fatigue behavior, Addit. Manuf. 47 (2021) 102292.
[29] Q. Hua, R. Li, M. Wang, H. Zhu, X. Liu, D. Lai, J. Li, T. Yuan, High cycle fatigue property of Al–Mg–Sc–Zr alloy fabricated by laser powder bed fusion, Adv. Eng. Mater. 25 (17) (2023) 2300352.
[30] P. He, R.F. Webster, V. Yakubov, H. Kong, Q. Yang, S. Huang, M. Ferry, J.J. Kruzic, X. Li, Fatigue and dynamic aging behavior of a high strength Al-5024 alloy fabricated by laser powder bed fusion additive manufacturing, Acta Mater. 220 (2021) 117312.
[31] Z. Qin, N. Kang, M. El Mansori, Z. Wang, H. Wang, X. Lin, J. Chen, W. Huang, Anisotropic high cycle fatigue property of Sc and Zr-modified Al-Mg alloy fabricated by laser powder bed fusion, Addit. Manuf. 49 (2022) 102514.
[32] Z. Qin, N. Kang, H. Zong, C. Zhan, Y. Fang, Z. Wang, M. El Mansori, J. Chen, X. Lin, W. Huang, Improved fatigue properties of laser powder bed fusion of Al–4.74 Mg–0.70 Sc–0.32 Zr alloy via hot isostatic pressing, Materials Research Letters 10 (11) (2022) 720–727.
[33] L. Meng, A. Goyal, V. Doquet, N. Ranc, J.-P. Couzinié, Ultrafine versus coarse grained Al 5083 alloys: from low-cycle to very-high-cycle fatigue, Int. J. Fatig. 121 (2019) 84–97.
[34] M.S. Kaiser, K.M. Shorowordi, H.M.M. Al Rashed, Effect of rolling on the fractional recrystallization behaviour of Al-Mg and Al-Mg-Zr alloys, J. Mech. Eng. 48 (1) (2018) 24–29.
[35] J.R. Croteau, J.-G. Jung, S.A. Whalen, J. Darsell, A. Mello, D. Holstine, K. Lay, M. Hansen, D.C. Dunand, N.Q. Vo, Ultrafine-grained Al-Mg-Zr alloy processed by shear-assisted extrusion with high thermal stability, Scr. Mater. 186 (2020) 326–330.
[36] EOS aluminum Al5X1 datasheet. https://www.eos.info/05-datasheet-images/Assets_MDS_Metal/EOS_Aluminium_Al5X1/Material_DataSheet_EOS_Aluminium_Al5X1_EN.pdf, 2023.
[37] X. Li, Y. Liu, Effect of laser remelting on printability, microstructure and mechanical performance of Al-Mg-Sc-Zr alloy produced by laser powder bed fusion, J. Alloys Compd. 963 (2023) 171287.
[38] X. Li, Y. Liu, Microstructure characterization and mechanical performance of laser powder bed fusion processed AlMgScZr alloy: effect of heat treatment, Mater. Sci. Eng., A 862 (2023) 144501.
[39] H. Zhang, H. Liu, Y. Li, F. Chu, Q. Hu, X. Wu, H. Rao, S. Cao, Anisotropic tensile creep behavior in laser powder bed fusion manufactured Al–Mn–Mg–Sc–Zr alloy, J. Mater. Res. Technol. 28 (2024) 2071–2076.
[40] D. Schliephake, C. Lopes, Y.M. Eggeler, H. Chen, J. Freudenberger, D. Bayoumy, A. J. Huang, A. Kauffmann, Improved work hardening capability and ductility of an additively manufactured and deformed Al-Mn-Mg-Sc-Zr alloy, J. Alloys Compd. 924 (2022) 166499.
[41] B. Schuh, R. Pippan, A. Hohenwarter, Tailoring bimodal grain size structures in nanocrystalline compositionally complex alloys to improve ductility, Mater. Sci. Eng., A 748 (2019) 379–385.
[42] D. Mao, Y. Xie, X. Meng, X. Zhang, X. Ma, Z. Zhang, X. Sun, Y. Huang, Bimodal-grain structure enables superior strength-ductility synergy of pure Al, J. Alloys Compd. (2024) 175114.

[43] R.-Z. Wang, L.-Y. Cheng, S.-P. Zhu, P.-C. Zhao, H. Miura, X.-C. Zhang, S.-T. Tu, Semi-quantitative creep-fatigue damage analysis based on diffraction-based misorientation mapping and the correlation to macroscopic damage evolutions, Int. J. Fatig. 149 (2021) 106227.

[44] M.N. Gussev, K.J. Leonard, In situ SEM-EBSD analysis of plastic deformation mechanisms in neutron-irradiated austenitic steel, J. Nucl. Mater. 517 (2019) 45–56.

[45] M.D. Sangid, The physics of fatigue crack initiation, Int. J. Fatig. 57 (2013) 58–72.

[46] Y. Du, W. Huo, J. Xu, W. Zhang, Mechanical behavior and strengthening mechanisms in precipitation-strengthened aluminum alloy with gradient structure induced by sliding friction treatment, Metall. Mater. Trans. 51 (2020) 6207–6221.

[47] F. Belelli, R. Casati, C. Andrianopoli, F. Cuccaro, M. Vedani, Investigation and characterization of an Al-Mg-Zr-Sc alloy with reduced Sc content for laser powder bed fusion, J. Alloys Compd. 924 (2022) 166519.

[48] C. Colombo, A. Tridello, A.P. Pagnoncelli, C.A. Biffi, J. Fiocchi, A. Tuissi, L. M. Vergani, D.S. Paolino, Efficient experimental methods for rapid fatigue life estimation of additive manufactured elements, Int. J. Fatig. 167 (2023) 107345.

[49] R. Schwab, V. Ruff, On the nature of the yield point phenomenon, Acta Mater. 61 (5) (2013) 1798–1808.

[50] Y. Murakami, Effects of small defects and nonmetallic inclusions on the fatigue strength of metals, JSME international journal. Ser. 1, Solid mechanics, strength of materials 32 (2) (1989) 167–180.

[51] Y. Murakami, S. Nemat-Nasser, Growth and stability of interacting surface flaws of arbitrary shape, Eng. Fract. Mech. 17 (3) (1983) 193–210.

[52] Y. Murakami, Analysis of an arbitrarily shaped surface crack and stress field at crack front near surface, Transactions of the Japan Society of Mechanical Engineers, Series A 51 (464) (1985) 1050–1056.

[53] Y. Murakami, S. Kodama, S. Konuma, Quantitative evaluation of effects of non-metallic inclusions on fatigue strength of high strength steels. I: basic fatigue mechanism and evaluation of correlation between the fatigue fracture stress and the size and location of non-metallic inclusions, Int. J. Fatig. 11 (5) (1989) 291–298.

[54] Y. Murakami, Metal Fatigue: Effects of Small Defects and Nonmetallic Inclusions, Academic Press, 2019.

[55] A. Tridello, VHCF response of Gaussian specimens made of high-strength steels: comparison between unrefined and refined AISI H13, Fatig. Fract. Eng. Mater. Struct. 40 (10) (2017) 1676–1689.

[56] A. Tridello, C. Boursier Niutta, M. Rossetto, F. Berto, D.S. Paolino, Statistical models for estimating the fatigue life, the stress–life relation, and the P-S–N curves of metallic materials in Very High Cycle Fatigue: a review, Fatig. Fract. Eng. Mater. Struct. 45 (2) (2022) 332–370.